AN INDEPENDENT MEASUREMENT OF THE INCIDENCE OF Mg II ABSORBERS ALONG GAMMA-RAY BURST SIGHT LINES: THE END OF THE MYSTERY?

The Astrophysical Journal, 773:82 (24pp), 2013 August 20 doi:10.1088/0004-637X/773/2/82

AN INDEPENDENT MEASUREMENT OF THE INCIDENCE OF Mg II ABSORBERS ALONG GAMMA-RAY BURST SIGHT LINES: THE END OF THE MYSTERY?

A. Cucchiara[1], J. X. Prochaska[1], G. Zhu[2], B. Ménard[2,3,14], J. P. U. Fynbo[4], D. B. Fox[5], H.-W. Chen[6], K. L. Cooksey[7], S. B. Cenko[8], D. Perley[9], J. S. Bloom[8], E. Berger[10], N. R. Tanvir[11], V. D'Elia[12], S. Lopez[13], R. Chornock[10], and T. de Jaeger[13]

[1] Department of Astronomy and Astrophysics, UCO/Lick Observatory, University of California, 1156 High Street, Santa Cruz, CA 95064, USA; acucchia@ucolick.org
[2] Department of Physics and Astronomy, Johns Hopkins University, Baltimore, MD 21218, USA
[3] Kavli Institute for the Physics and Mathematics of the Universe, Tokyo University, Kashiwa 277-8583, Japan
[4] Dark Cosmology Centre, Niels Bohr Institute, University of Copenhagen, Juliane Maries Vej 30, DK-2100 Copenhagen, Denmark
[5] Department of Astronomy and Astrophysics, Pennsylvania State University, University Park, PA 16802, USA
[6] Department of Astronomy and Astrophysics, Kavli Institute for Cosmological Physics, University of Chicago, Chicago, IL 60637, USA
[7] MIT Kavli Institute for Astrophysics and Space Research, 77 Massachusetts Avenue, 37-685, Cambridge, MA 02139, USA
[8] Department of Astronomy, University of California, Berkeley, CA 94720-3411, USA
[9] Department of Astronomy, California Institute of Technology, MC 249-17, 1200 East California Blvd., Pasadena, CA 91125, USA
[10] Harvard-Smithsonian Center for Astrophysics, 60 Garden Street, Cambridge, MA 02138, USA
[11] Department of Physics and Astronomy, University of Leicester, University Road, Leicester LE1 7RH, UK
[12] Istituto Nazionale di Astrofisica-Osservatorio Astronomico di Roma, Via di Frascati 33, I-00040 Monte Porzio Catone (RM), Italy
[13] Departamento de Astronomía, Universidad de Chile, Casilla 36-D, Santiago, Chile
Received 2012 November 27; accepted 2013 May 25; published 2013 July 29

ABSTRACT

In 2006, Prochter et al. reported a statistically significant enhancement of very strong Mg II absorption systems intervening the sight lines to gamma-ray bursts (GRBs) relative to the incidence of such absorption along quasar sight lines. This counterintuitive result has inspired a diverse set of astrophysical explanations (e.g., dust, gravitational lensing) but none of these has obviously resolved the puzzle. Using the largest set of GRB afterglow spectra available, we reexamine the purported enhancement. In an independent sample of GRB spectra with a survey path three times larger than Prochter et al., we measure the incidence per unit redshift of $\geqslant$1 Å rest-frame equivalent width Mg II absorbers at $z \approx 1$ to be $\ell(z) = 0.18 \pm 0.06$. This is fully consistent with current estimates for the incidence of such absorbers along quasar sight lines. Therefore, we do not confirm the original enhancement and suggest those results suffered from a statistical fluke. Signatures of the original result do remain in our full sample ($\ell(z)$ shows an $\approx$1.5 enhancement over $\ell(z)_{\rm QSO}$), but the statistical significance now lies at $\approx$90% c.l. Restricting our analysis to the subset of high-resolution spectra of GRB afterglows (which overlaps substantially with Prochter et al.), we still reproduce a statistically significant enhancement of Mg II absorption. The reason for this excess, if real, is still unclear since there is no connection between the rapid afterglow follow-up process with echelle (or echellette) spectrographs and the detectability of strong Mg II doublets. Only a larger sample of such high-resolution data will shed some light on this matter.

Key words: gamma-ray burst: general – quasars: absorption lines – techniques: spectroscopic

Online-only material: color figures

1. INTRODUCTION

In the last decade, the study of the intergalactic medium and circumgalactic medium (CGM) has received a great boost thanks to large spectroscopic surveys of distant quasars, in particular the data set provided by the Sloan Digital Sky Survey (SDSS; York et al. 2000). These objects randomly sample thousands of lines of sight and, being bright background sources of light, probe gas, and matter located in foreground objects.

One of the most commonly surveyed set of transitions in quasar spectra is the Mg II doublet at 2796 and 2803 Å. Its common detection stems from the large rest wavelength (which makes them easily detectable by most optical spectrographs when the absorber is located at redshift $z = 0.5$–2.2), the relatively high abundance of Mg, and the strength of this resonance-line doublet. The Mg II systems are frequently classified in terms of the rest-frame equivalent width, W_r, of the bluer component as "weak" ($W_{2796} < 0.3$ Å), "strong" ($W_{2796} > 0.3$ Å) as in Steidel & Sargent (1992) and Churchill et al. (1999), and "very strong" ($W_{2796} > 1.0$ Å, like in Rodríguez Hidalgo et al. 2012). For simplicity, throughout the paper we will refer to this last category as "strong," since it is the only one pertinent to this work. Mg II doublet lines have been surveyed extensively from $z \approx 0.1$–2.5 in the optical passband and now to $z = 5.2$ with near-IR spectroscopy (e.g., Steidel & Sargent 1992; Nestor et al. 2005; Prochter et al. 2006a; Quider et al. 2011; Simcoe et al. 2011; Zhu & Menard 2012). The results indicate that while the weak and strong absorbers incidence show small if any evolution with redshift, the very strong Mg II absorbers present an increasing trend up to $z \sim 3$ before declining at higher redshift (Prochter et al. 2006a; Matejek & Simcoe 2012). This evolution rather closely tracks the cosmic star formation history (Prochter et al. 2006a; Zhu & Menard 2012), suggesting that some systems may be causally connected to ongoing star formation (Ménard et al. 2011; Matejek & Simcoe 2012), although accurate analysis of the SDSS survey needs to be carefully taken into account in order to avoid technical biases (López & Chen 2012).

For several decades now, strong Mg II absorption has been associated with gas in and around galaxies. Early work identified a small sample of $L \approx L^*$ galaxies at modest impact parameters ($\rho \approx 10$–50 kpc) to quasars exhibiting strong Mg II absorption (Bergeron 1986; Lanzetta et al. 1987; Steidel 1993), although no

[14] Alfred P. Sloan fellow.

Table 1
List of Objects Considered for the Mg II Analysis

GRB	z_{GRB}	Telescope	Instrument	Resolution (Å)	S/N[a]	Reference
111229A	1.380	Gemini	GMOS	5.8	6.7	This work
111107A	2.893	Gemini	GMOS	5.8	3.5	This work
111008A	4.989	Gemini	GMOS	5.8	3.8	This work
110918A	0.982	Gemini	GMOS	5.8	20	This work
110731A	2.830	Gemini	GMOS	5.8	26	This work
110726A	1.036	Gemini	GMOS	5.8	9	This work
110213B	1.083	Gemini	GMOS	3.4	5	This work
110213A	1.460	Bok	FAST	6	20	(4)
110205A	2.214	Lick	KAST	11	14	(4)
100906A	1.727	Gemini	GMOS	5.8	21	This work
100901A	1.408	Gemini	GMOS	3.4	6	This work
100814A	1.438	MAGELLAN	MagE	1.8	10	This work
100513A	4.798	Gemini	GMOS	5.8	17	This work
100418A	0.624	VLT	X-Shooter	0.86/0.72/2*	12–38	(19)
100414A	1.368	Gemini	GMOS	5.8	11	This work
100302A	4.813	Gemini	GMOS	5.8	3	This work
100219A	4.667	Gemini	GMOS	1.6	1.2	This work
091208B	1.063	Gemini	GMOS	5.8	26	(2)
091109A	3.076	VLT	FORS2	13	3	This work
091029	2.752	Gemini	GMOS	5.8	39	This work
091024	1.092	Gemini	GMOS	5.8	55	(2)
091020A	1.713	NOT	ALFOSC	13	7	This work
090926A	2.106	VLT	X-Shooter	1.0	15–30	(6)
090902B	1.822	Gemini	GMOS	4	14	This work
090812A	2.454	VLT	FORS2	13	15	(18)
090529A	2.625	VLT	FORS2	13	4	(18)
090519A	3.851	VLT	FORS2	13	3	(18)
090516A	4.109	VLT	FORS2	13	24	(18)
090426	2.609	Keck	LRIS	5.5	8	This work
090424	0.544	Gemini	GMOS	5.8	22	This work
090323	3.567	Gemini	GMOS	5.8	17	This work
090313	3.375	Gemini	GMOS	5.8	11	This work
081222	2.771	Gemini	GMOS	5.8	21	This work
081029	3.847	Gemini	GMOS	5.8	42	(2)
081008	1.967	Gemini	GMOS	3.4	35	(2)
081007	0.529	Gemini	GMOS	5.8	31	(2)
080928	1.690	Gemini/VLT	GMOS/FORS2	5.8/13	8/25	(2)/(3)
080916A	0.689	VLT	FORS1	13	5	(18)
080913A	6.700	VLT	FORS2	13	2.5	(13)
080905B	2.374	VLT	FORS1	13	13	(18)
080810	3.350	Keck	HIRES	0.18	16	(18)
080805	1.505	VLT	FORS2	13	3	(3)
080804	2.205	Gemini	GMOS	5.8	17	(2)
080721	2.608	TNG	Dolores	8.1	9	(18)
080710	0.845	Gemini	GMOS	3.4	35	(2)
080707	1.234	VLT	FORS1	13	5	(3)
080607	3.036	Keck	LRIS	4	11	(3)
080605A	1.639	VLT	FORS2	13	30	(3)
080604	1.416	Gemini	GMOS	5.8	4	(2)
080603B	2.686	NOT	ALFOSC	13	41	(3)
080603A	1.688	Gemini	GMOS	5.8	38	(2)
080520	1.545	VLT	FORS2	13	5	(3)
080413B	1.100	Gemini	GMOS	3.4	2	(2)
080413A	2.433	Gemini	GMOS	4	14	(2)/(9)
080411	1.030	VLT	FORS1	13	60	(18)
080330	1.513	NOT	ALFOSC	13	18	(3)
080319C	1.949	Gemini	GMOS	3.4	4	(2)
080319B	0.937	Gemini/VLT	GMOS/UVES	5.8/0.13	45/70	(2)/(9)
080310A	2.4272	VLT	UVES	0.13	15	(9)
080210	2.6419	VLT	FORS2	13	33	(3)
071122	1.141	Gemini	GMOS	5.8	12	(2)
071117	1.334	VLT	FORS1	13	4	(3)
071112C	0.823	Gemini	GMOS	4	3	(2)
071031	2.692	VLT	UVES/FORS2	0.13/13	70/40	(3)
071020	2.145	VLT	FORS2	13	6	(3)

Table 1
(Continued)

GRB	z_{GRB}	Telescope	Instrument	Resolution (Å)	S/N[a]	Reference
071010B	0.947	Gemini	GMOS	5.8	15	(2)
071003	1.6044	Keck	LRIS	5	34	(20)
070810A	2.170	Keck	LRIS	5	6	(21)
070802	2.453	VLT	FORS2	13	8	(3)
070721B	3.626	VLT	FORS2	13	6	(18)
070611	2.039	VLT	FORS2	13	15	(3)
070529	2.498	Gemini	GMOS	3.4	12	(2)
070506	2.306	VLT	FORS1	13	3	(3)
070411	2.954	VLT	FORS1	13	6.5	(3)
070318	0.836	Gemini	GMOS	4	8	(2)
070306	1.496	VLT	FORS2	13	4	(3)
070125	1.547	Gemini/VLT	GMOS/FORS1	5.8/	6/15	(10)/(3)
070110	2.352	VLT	FORS2	13	30	(3)
061121	1.314	Keck	LRIS	13	28	(3)
061110B	3.434	VLT	FORS1	13	11	(3)
061110A	0.758	VLT	FORS1	13	6	(3)
061007	1.261	VLT	FORS1	13	6	(3)
060927	5.468	VLT	FORS1	8	2.5	(1)
060926	3.205	VLT	FORS1	13	8	(1)
060908	1.884	Gemini	GMOS	5.8	8	This work
060906	3.686	VLT	FORS1	13	5.8	(1)
060904B	0.703	VLT	FORS1	13	12	(18)
060729	0.543	Gemini	GMOS	3.4	26	(2)
060714	2.711	VLT	FORS1	13	50	(3)
060708	1.923	VLT	FORS2	13	5	(3)
060707	3.425	VLT	FORS2	13	7	(3)
060607A	3.047	VLT	UVES	0.13	43	(9)
060526	3.221	VLT	FORS1	13	38	(1)
060522	5.111	Keck	LRIS	5	2.3	(1)
060512	2.092	VLT	FORS1	13	3	(3)
060510B	4.922	Gemini	GMOS	5.8	8.4	(2)
060502A	1.515	Gemini	GMOS	5.8	8	(2)
060418	1.489	Gemini/VLT	GMOS/UVES	5.8/0.13	86/60	(2)/(11)
060210	3.912	Gemini	GMOS	5.7	26	(2)
060206	4.046	NOT	ALFOSC	13	40	(3)
060124	2.296	Keck	ESI	13	8	(3)
060115	3.5328	VLT	FORS1	13	10	(3)
051111	1.5489	Keck	HIRES	0.18	20	(12)
050922C	2.1996	VLT	UVES	0.13	12	(9)
050908	3.339	Gemini/Keck	GMOS/Deimos	4/1.6	9/12	(2)/This work
050820	2.614	VLT	UVES	0.13	23	(9)
050802	1.711	NOT	ALFOSC	13	7	(3)
050801	1.559	Keck	LRIS	5	5	(3)
050730	3.9687	VLT	UVES	0.13	40	(9)
050401	2.896	VLT	FORS2	13	23	(3)
050319	3.240	NOT	ALFOSC	13	6	(3)
030429	2.655	VLT	FORS1	13	7	(1)
030323	3.372	VLT	FORS1	13	8	(13)
030226	1.986	VLT	FORS1	13	30	(14)
021004	2.323	VLT	UVES	0.13	40	(9)
020813	1.255	VLT	UVES	0.13	60	(15)
010222	1.477	Keck	ESI	0.6	4	(16)
000926	2.038	Keck	ESI	0.6	12	(17)

Notes. [a] Signal-to-noise ratio is estimated as the median at the continuum level over a wavelength range clean of telluric lines.

References. (1) Jakobsson et al. 2006; (2) Cucchiara 2010; (3) Fynbo et al. (2009) and references therein; (4) Cucchiara et al. 2011a; (5) de Ugarte Postigo et al. 2011; (6) D'Elia et al. 2010; (7) D'Elia et al. 2011; (8) Thoene et al. 2008; (9) Vergani et al. 2009; (10) Cenko et al. 2008; (11) Vreeswijk et al. 2007; (12) Prochaska et al. 2007; (13) Vreeswijk et al. 2004; (14) Klose et al. 2004a; (15) Barth et al. 2003; (16) Mirabal et al. 2002; (17) Castro et al. 2003; (18) de Ugarte Postigo et al. 2012; (19) de Ugarte Postigo et al. 2011; (20) Perley et al. 2008; (21) Milvang-Jensen et al. 2012.

Table 2
Studied Sample

	Number[a] of GRBs	$\Delta z_{1.0\,\text{Å}}$	$N_{1.0\,\text{Å}}$	$\ell_{\text{GRB}}(z)$	$\ell_{\text{QSO}}(z)$
Sample I	83	44.9	8	0.18 ± 0.06	0.26
Sample F	95	55.5	20	0.36 ± 0.09	0.24
Sample H	18	20.3	13	0.64 ± 0.18	0.25
Sample L	79	35.3	7	0.19 ± 0.08	0.24

Notes. Summary of our Mg II search: the sample name and the number of lines of sight included are listed in the first two columns; the total redshift path density explored and the number of absorbers identified are listed in the third and forth columns. Based on these, we could determine the incidence of the absorbers in each sample and compare it with the expected incidence along our QSOs sample (last column).
[a] The total number of GRB lines of sight in each sample corresponds to the sum of all those GRBs where $\ell(z) \neq 0$.

significant trend has been found for a population of luminous red galaxies (e.g., Bowen & Chelouche 2011 and references therein).

These observations motivate the association of Mg II gas with the outer disk and/or CGM of these galaxies. Several QSO lines of sight presenting Mg II absorbers have been explored in order to probe the extent and the baryon content around low-z galaxies (Kacprzak et al. 2012; Chen & Tinker 2008 and references therein), as well as a diagnostic of the inner part of these galaxies' interstellar medium (Bowen et al. 1995). Also, a stack analysis was performed by Zibetti et al. (2007) using light profiles (from associated galaxies) of quasars exhibiting strong Mg II absorption in the SDSS. With their image-stacking technique they studied the cross-correlation between the Mg II gas and the galaxy light from 10 to 200 kpc, finding that strong Mg II absorbers may be explained by models that include metal-enriched outflows from star-forming/bursting galaxies. Most recently, several attempts to trace the covering fraction and nature of Mg II absorption by targeting known galaxies with coincident background quasars have been performed (Barton & Cooke 2009; Chen et al. 2010; Werk et al. 2012). Their results indicate the mean covering fraction increases from ∼70% for $W_r \geqslant 0.3$ Å to ∼80% for $\geqslant$0.1 Å, confirming that extended Mg II absorbing halos are a common feature around normal galaxies. Finally, it has been found that "strong" absorbers are often associated with nearby (within 75 kpc) ~ 0.1–$5\,L^*$ galaxies along the line of sight (Kacprzak et al. 2008; Nestor et al. 2011; Chen et al. 2010).

The survey and analysis of Mg II gas is no longer limited to quasar spectroscopy. For example, researchers have now used distant galaxies to probe foreground galaxies, enabling searches at very small impact parameter (Rubin et al. 2011) and statistical "maps" of the absorption correlated with the foreground galaxy orientation (Bordoloi et al. 2011; Kacprzak et al. 2012). Similarly, gamma-ray bursts (GRBs) with their extraordinarily bright optical afterglows provide not only direct information on their host galaxies, but also trace matter intercepting their lines of sight (Metzger et al. 1997).

The advantage of using GRBs as background sources is twofold: first, they can be observed up to very high redshifts (Kawai et al. 2006; Tanvir et al. 2009; Salvaterra et al. 2009; Cucchiara et al. 2011b), which allows one to explore a larger redshift path length, and second, their discovery is largely unbiased with respect to intrinsic properties of their hosts (extinction, luminosity, or mass). When a GRB fades away, they leave the lines of sight clear for future deep observations in order to search for the Mg II counterparts (Vreeswijk et al. 2003; Jakobsson et al. 2004; Schulze et al. 2012; Chen 2012). One of the first attempts to identify the nature of three absorbers along GRB 060418 was performed by Pollack et al. (2009), which identified the absorbers to be $L \sim 0.1$–$1\,L^*$ galaxies at very small impact parameter from the GRB location ($\rho \lesssim 10\,h^{-1}$ kpc). Deep imaging of several other fields have confirmed these early findings (Chen et al. 2009). On the other hand, the number of GRBs discovered and spectroscopically observed is several orders of magnitude less then the number of quasars available in large optical surveys (e.g., SDSS DR8). This difference has been reduced, however, with the success of the *Swift* satellite providing the discovery and follow-up of several hundred GRBs (Gehrels et al. 2004, 2009).

Shortly after the launch of *Swift* in 2004 November, a survey of Mg II absorption in GRB afterglow spectroscopy was performed for an early sample of *Swift* bursts and a heterogeneous sample of pre-existing GRB spectra (Prochter et al. 2006b, hereafter P06). The authors revealed an extremely puzzling result: the incidence of strong ($W_{2796} \geqslant 1$ Å) intervening Mg II absorbers was about four times higher along GRB sight lines than quasar sight lines. Despite the small sample size, the statistical significance of their data set was high: the null hypothesis that GRBs and quasar spectra would show identical incidences of strong, foreground Mg II absorption was ruled out at $\gtrsim$99.99% confidence. Furthermore, no such excess was found in other common class of absorbers, e.g., C IV features

Table 3
List of Excluded Lines and Regions in the Redshift Path-length Estimate

Description	λ_{rest} (Å)	Description	λ_{rest} (Å)
N V	1238, 1242	C I	1560
S II	1250, 1253, 1259	Fe II	1608, 1611, 2249, 2260, 2344, 2374, 2382, 2586, 2600
Si II	1260, 1304, 1526, 1808	Al II	1670
Si II*	1264, 1309, 1533, 1816	Al III	1854, 862
O I	1302	Cr II	2017, 2026, 2056, 2066
Ni II	1317, 1370, 1454, 1703, 1709, 1741, 1751	Zn II	2026, 2062
C II	1334	Ni II*	2217
C II*	1335	Mn II	2576, 2594, 2606
Si IV	1393, 1402	Band B[a]	6860–7000
C IV	1548, 1550	Band A[a]	7600–7704
Atm. Band[a]	8130–8323	Atm. Band[a]	8930–9020

Notes. [a] Atmospheric absorption bands from the HIRES telluric line list: http://www2.keck.hawaii.edu/inst/common/makeewww/Atmosphere/atmabs.txt. The indicated wavelengths are (obviously) independent of the GRB redshift.

Table 4
Searchable Redshifts Intervals ($g(z) = 1$) Along GRB 030226 Sight Line

GRB	z_{GRB}	z_{start}	z_{end}	Δz^{cum}
030226	1.986	0.412018	0.420601	0.00858259
		0.444918	0.457792	0.0214566
		0.460653	0.462083	0.0228871
		0.474957	0.475673	0.0236024
		0.480679	0.481394	0.0243176
		0.495699	0.497129	0.0257480
		0.499275	0.508573	0.0350459
		0.509288	0.510003	0.0357610
		0.511433	0.512149	0.0364761
		0.513579	0.515010	0.0379065
		0.515725	0.526453	0.0486348
		0.537181	0.548625	0.0600783
		0.552201	0.552916	0.0607935
		0.555062	0.557207	0.0629392
		0.557923	0.558638	0.0636543
		0.562929	0.565790	0.0665151
		0.572227	0.572942	0.0672303
		0.573657	0.574373	0.0679455
		0.577233	0.577949	0.0686607
		0.584386	0.591538	0.0758129
		0.592968	0.597260	0.0801042
		0.597975	0.598690	0.0808195
		0.601551	0.602266	0.0815347
		0.609418	0.614425	0.0865412
		0.615140	0.617286	0.0886868
		0.620862	0.621577	0.0894020
		0.667351	0.695244	0.117295
		0.695960	0.696675	0.118011
		0.698105	0.712410	0.132315
		0.718847	0.719562	0.133030
		0.721707	0.723853	0.135176
		0.724568	0.725284	0.135891
		0.728144	0.728860	0.136606
		0.729575	0.738157	0.145189
		0.741018	0.742449	0.146619
		0.745310	0.778210	0.179519
		0.781070	0.783216	0.181665
		0.785362	0.786792	0.183095
		0.788223	0.788938	0.183810
		0.791799	0.794660	0.186671
		0.795375	0.796805	0.188102
		0.797520	0.799666	0.190247
		0.801097	0.803957	0.193108
		0.806818	0.808249	0.194539
		0.822553	0.824699	0.196684
		0.826844	0.834712	0.204552
		0.841149	0.844010	0.207413
		0.845440	0.847586	0.209558
		0.848301	0.851162	0.212419
		0.852592	0.853307	0.213134
		0.856884	0.859029	0.215280
		0.861175	0.864751	0.218856
		0.868327	0.869042	0.219571
		0.873333	0.875479	0.221717
		0.879055	0.881201	0.223863
		0.881916	0.889068	0.231015
		0.890499	0.893360	0.233875
		0.894790	0.898366	0.237451
		0.899081	0.899797	0.238167
		0.902657	0.907664	0.243173
		0.912670	0.914101	0.244604
		0.914816	0.916962	0.246749
		0.917677	0.924829	0.253901
		0.927690	0.929836	0.256047
		0.937703	0.938418	0.258193
		0.954868	0.955584	0.258908

Table 4
(Continued)

GRB	z_{GRB}	z_{start}	z_{end}	Δz^{cum}
		0.961305	0.963451	0.261054
		0.966312	0.974894	0.269636
		1.00279	1.02639	0.293238
		1.02854	1.03068	0.295384
		1.03140	1.03497	0.298960
		1.03551	1.03622	0.299675
		1.03765	1.04695	0.308973
		1.04910	1.04981	0.309689
		1.05053	1.07199	0.331145
		1.08128	1.08557	0.335436
		1.08915	1.11204	0.358323
		1.11418	1.11561	0.359754
		1.11776	1.11990	0.361900
		1.12062	1.12205	0.363330
		1.12634	1.12849	0.365475
		1.12992	1.14136	0.376919
		1.14279	1.14780	0.381925
		1.15137	1.15280	0.383356
		1.15638	1.15710	0.384071
		1.16639	1.16782	0.385501
		1.16854	1.17855	0.395514
		1.17927	1.18141	0.397660
		1.18213	1.18499	0.400521
		1.18570	1.18857	0.403382
		1.19286	1.19429	0.404812
		1.20430	1.20502	0.405527
		1.20788	1.26509	0.462745
		1.26581	1.29013	0.487062
		1.29084	1.31373	0.509949
		1.31516	1.31659	0.511380
		1.31802	1.31874	0.512095
		1.31945	1.32303	0.515671
		1.32446	1.33232	0.523538
		1.34234	1.36022	0.541419
		1.36379	1.36665	0.544280
		1.36952	1.39455	0.569312
		1.39884	1.40099	0.571458
		1.40456	1.40671	0.573604
		1.41028	1.41314	0.576464
		1.41600	1.44747	0.607934
		1.48252	1.48467	0.610080
		1.48824	1.48896	0.610795
		1.50898	1.50970	0.611510
		1.51757	1.52400	0.617947
		1.53259	1.53402	0.619377
		1.54045	1.54188	0.620807
		1.54617	1.56763	0.642264
		1.57049	1.57121	0.642979
		1.57192	1.60125	0.672303
		1.60196	1.60554	0.675879
		1.60625	1.66204	0.731666
		1.66275	1.67634	0.745255
		1.67777	1.69065	0.758129
		1.69136	1.70853	0.775295
		1.76718	1.76789	0.776010
		1.77361	1.77433	0.776725
		1.77934	1.78148	0.778871
		1.78577	1.80151	0.794605
		1.80222	1.80365	0.796036
		1.80508	1.80580	0.796751
		1.80651	1.80723	0.797467
		1.80794	1.80937	0.798897
		1.81009	1.82225	0.811056
		1.83298	1.83441	0.812486
		1.83584	1.83798	0.814632
		1.84084	1.84227	0.816062

Table 4
(Continued)

GRB	z_{GRB}	z_{start}	z_{end}	Δz^{cum}
		1.84299	1.86159	0.834658
		1.86302	1.87660	0.848247
		1.87732	1.87804	0.848962
		1.87875	1.89949	0.869704

Notes. In this table, we present the different interval ($z_{start} - z_{end}$) for which we estimate $g(z) = 1$, after accounting for skylines, GRB host lines and for which we are confident we are able to detect an Mg II blue component with $W_r(2796) \geqslant 1$ Å at 5σ level. The last column (Δz^{cum}) shows the cumulative redshift path length probed along the GRB sight lines.

(Tejos et al. 2007) or for weak Mg II absorbers (Tejos et al. 2009).

In P06, the authors proposed several hypotheses that might explain the difference, which have since been studied in greater detail: (1) a possible intrinsic origin of these absorbers associated near the GRBs themselves (Cucchiara et al. 2009; Bergeron et al. 2011), (2) a significant dust bias along QSO lines of sight (Ménard et al. 2008; Porciani et al. 2007a; Budzynski & Hewett 2011), (3) a geometric effect difference due to the sizes of the emitting regions between GRBs and QSOs (Stocke & Rector 1997; Frank et al. 2007; Porciani et al. 2007a; Lawther et al. 2012), and (4) a gravitational lensing effect (Vergani et al. 2009; Porciani & Madau 2001; Rapoport et al. 2012, 2013). Some of these works have ruled out several of these possibilities and none appears to be sufficient on its own to explain the observations. After 7 years of the *Swift* mission and more than 200 GRBs with spectroscopic confirmations, this mystery remains.

It is important to emphasize that the original P06 work, and even the studies that have followed, have relied on a small sample of GRB afterglow spectra. Even the largest analysis to date analyzed only 26 lines of sight (finding 22 absorbers) for a total redshift path of $\Delta z = 31.55$ (Vergani et al. 2009). Furthermore, no study has analyzed a completely independent set of GRB sight lines from the P06 analysis.

In this paper, we use data obtained primarily during the *Swift* era by several facilities to obtain the most complete sample of GRB afterglow spectra and the largest redshift path length available to date. From this parent sample, we are able to construct subsamples which are entirely independent from the original work of P06. Similarly, we can study possible instrumental biases (e.g., spectral resolution) which may affect the final results.

The paper is structured as follows. In Section 2 we describe our data set and the data analysis procedure, while in Section 3 we present our procedure for defining the redshift path density per GRB sight line. Section 4 describes the search methodology to identify possible Mg II systems along every line of sight, with distinction between different data sets (e.g., high resolution versus low resolution, strong versus weak Mg II equivalent width). Finally, in Sections 5 and 6 we present our findings, including interesting subsamples results, and we summarize them in light of possible steps forward into understanding this puzzling phenomenon. All the quoted errors, unless otherwise stated, are considered at 1σ confidence level.

2. DATA SELECTION

The acquisition of an optical spectrum from a given GRB afterglow is a complex and unrepeatable process. During the *Swift* era, the time lapse between the discovery of the gamma-ray emission (by the *Swift*/BAT instrument) and the afterglow localization (by X-Ray Telescope (XRT) and/or UVOT on board the spacecraft) is generally less than a few minutes, with some exceptions due to observability constraints which delay the satellite to slew toward the BAT position (e.g., due to the small angular separation between the GRB and the Moon or the Sun).

The on board localization has an accuracy between several arcminutes (BAT only) to subarcseconds (UVOT) and the immediate transmission to the ground of all the *Swift*-acquired data via the Gamma-Ray Burst Network (Barthelmy et al. 1995) allows rapid (seconds to hours) follow-up with ground-based optical/IR telescopes.

In most of the cases presented in this paper, rapid follow-up spectroscopic observations were triggered as soon as an X-ray counterpart position was delivered (XRT identified more than 98% of the BAT GRBs) often via target of opportunity (ToO) programs at 8 m class facilities.

In other cases, especially for high-z bursts, robotic, real-time follow-up by different facilities have provided similarly accurate identification within the first hour, using redder filters than the ones available on *Swift*/UVOT (e.g., the GROND and RAPTOR instruments; Greiner et al. 2008; Vestrand et al. 2002). Due to the prompt responses, different groups have been able to obtain spectroscopic observations of the optical afterglow when it was bright enough to detect absorption lines, which generally yield a definitive estimate of the GRB redshift. For this purpose, the identification of fine-structure lines represents a secure determination of the GRBs host galaxies and the GRB circumstellar environment (Prochaska et al. 2006). Other secure identification is the presence of a damped Lyα system, which also has been signature of a typical high-z GRB host galaxy environment. Whenever these features are not present, we assume that the higher redshift system of absorption features from several ionized transitions corresponds to the GRB redshift, but obviously does not guarantee that these features do not rise, instead, in foreground objects along the GRB line of sight (see, for example, GRB 071003; Perley et al. 2008).

For GRBs that occurred before the launch of the *Swift* satellite, a similar procedure was followed though the slower response of the space observatories delayed the spectroscopic observations of several hours, precluding the possibility of obtaining a large sample of early, high signal-to-noise (S/N) spectra.

Since the goal of this paper is to construct the largest compilation of GRB afterglow spectra from which we investigate the presence of strong Mg II absorbers, we constructed our parent sample collecting the optical afterglow spectra for all long GRBs with reported redshifts, restricted as follows: because of our interest in detecting Mg II lines, and because most spectrographs have wavelength coverage beginning at ~3800 Å (or poor UV sensitivity), we require the Mg II doublet rest-frame wavelength to be redshifted beyond this limit. This leads us to include all the publicly available spectra obtained from GRBs with redshift higher than $z_{GRB} = 0.36$ (corresponding to 66% of all long GRBs with spectroscopic follow-up). No other selection criteria have been applied (as, for example, afterglow brightness or sky localization), since these would only reduce our surveyed path length and may introduce observational biases, complicating the comparison with the quasars sample.

The spectra analyzed in this paper were obtained with facilities across the world, including the Gemini Observatory, Keck Observatory, and Very Large Telescope (VLT).

Table 5
Intervening Systems

GRB	z_{GRB}	z_{abs}	$W_r(2796)$ (Å)	$W_r(2803)$ (Å)	Statistical Sample	Other Transition
010222	1.477	1.156	2.22(0.14)	1.69(0.11)	F, H	Fe II
020813	1.255	1.224	1.58(0.03)	1.43(0.03)	F, H	Mg I, Fe II
021004[a]	2.3295	0.555	0.66(0.045)	0.36(0.034)	N	Mg I, Fe II
		1.380	1.637(0.020)	1.574(0.043)	F, H	Mg I, Mn II, Fe II
		1.6026	1.407(0.024)	1.02(0.013)	F, H	Mg I, Fe II, Mn II
030226[b]	1.986	1.043	0.68(0.25)	0.41(0.25)	N	Al II
		1.963	2.22(0.10)	2.47(0.10)	N	Mg I, C IV, Si II
050730[a]	3.9687	1.7732	0.927(0.030)	0.718(0.016)	N	Mg I, Fe II
		2.2531	0.783(0.650)[c]	0.677(0.017)	N	Si II, Al II, Fe II, Mg I
050820[a]	2.6147	0.6915	2.723(0.007)	1.576(0.031)	F, H	Mg I
		1.4288	1.203(0.023)	1.265(0.026)	F, H	Mg I, Fe II, Al III
		1.6204	0.277(0.024)	0.214(0.008)	N	Mg I, Fe II, Zn II, Si II
		2.3598	0.424(0.306)[c]	0.517(0.024)	N	Fe II, Si II, Zn II, C IV
050908	3.339	1.548	1.21(0.02)	0.92(0.02)	F, H	Fe II
050922C[a]	2.1996	0.6369	0.187(0.018)	0.121(0.011)	N	Mg I, Fe II
		1.1076	0.476(0.029)	0.422(0.19)	N	Mg I, Fe II
		1.5670	0.121(0.080)[c]	0.088(0.007)	N	C IV, Fe II
051111	1.55	1.190	1.56(0.02)	1.92(0.01)	F, H	Mg I, Fe II
		0.827	0.39(0.02)	0.29(0.01)	N	Mg I
060418[c]	1.489	1.107	1.84(0.2)	1.58(0.1)	F, H	Mg I, Fe II, Zn II, Al III, Al II
		0.6559	1.52(0.3)	2.15(0.4)	F, H	Fe II
		0.603	1.49(0.2)	1.47(0.1)	F, H	Fe II
060502A	1.515	1.147	2.39(0.12)	2.87(0.12)	F, L, I	Mg I
		1.078	0.61(0.12)	0.49(0.12)	N	
		1.044	1.90(0.15)	1.92(0.16)	F, L, I	Fe I, Mn II, Mg I
060607A[a]	3.0748	1.5103	0.124(0.011)	0.144(0.007)	N	Fe II
		1.8033	1.916(0.006)	1.600(0.015)	F, H, I	Mg I, Fe II, Al III
		2.2783	0.210(0.058)	0.298(0.013)	N	Fe II, Al III, Al II, C IV, Si II, Si IV
060906	3.685	1.2659	1.63(0.28)[d]	1.63(0.28)[d]	N	Mg I
060926	3.2	0.924	2.49(0.62)[d]	2.49(0.62)[d]	N	Mg I, Fe I
		1.7954	3.27(0.69)	3.71(0.87)	N	Mg I, Fe II, Mn II
		1.8289	1.27(0.11)	0.72(0.07)	N	Mg I
061007	1.261	1.065	3.14(0.53)[c]	4.48(0.65)[c]	N	Mg I, Fe II, Mn II
070529	2.498	1.414	0.20(0.02)	0.09(0.02)	N	
070506	2.306	1.600	1.92(0.04)	1.65(0.05)	N	Al III
070611	2.039	1.297	2.65(0.27)	1.99(0.23)	N	Mg I, Fe II
070802	2.45	2.0785	0.82(0.12)	0.82(0.12)	N	Al II, Ni II, Mg I, Fe II
		2.2921	0.55(0.15)	0.55(0.22)	N	Ni II, Al III, Cr II, Fe II
071003	1.604	0.372	2.28(0.19)	1.91(0.19)	F, L, I	Mg I
		0.943	0.61(0.05)[b]	0.36(0.05)	N	Mg I
		1.101	0.80(0.06)	0.64(0.05)	N	Mg I
071031[a]	2.6922	1.0743	0.330(0.016)	0.206(0.008)	N	Fe II
		1.6419	0.806(0.014)	0.586(0.052)	N	Fe II, Al III, C IV
		1.9520	0.743(0.016)	0.612(0.016)	N	Mg I, Fe II
080310[a]	2.4272	1.6711	0.421(0.012)	0.366(0.016)	N	Mg I, Fe II, Al II, Si II, C IV
080319B[a]	0.9378	0.5308	0.614(0.001)	0.350(0.002)	N	Mg I, Fe II
		0.5662	0.083(0.003)	0.029(0.001)	N	Mg I, Fe II
		0.7154	1.482(0.001)	0.736(0.003)	F, H, I	Mg I, Fe II
		0.7608	0.108(0.002)	0.039(0.002)	N	Fe II
080319C	1.95	0.8104	2.04(0.52)	1.64(0.42)	N	Fe II, Mn II
080603A	1.688	1.271	3.11(0.11)	3.17(0.13)[c]	F, L, I	Mg I, Fe II
		1.563	0.77(0.01)	0.92(0.01)	N	Fe I
080605	1.64	1.2987	1.08(0.11)	0.77(0.10)	F, L, I	Fe II
080607A	3.036	1.341	3.0(0.08)	1.26(0.05)	F, L, I	Mg I
080805A	1.505	1.197	8.2(0.92)[d]	8.2(0.92)[d]	N	Mn II, Fe II
080905B	2.374	0.618	6.65(0.2)[d]	6.65(0.1)[d]	N	Mg I
080928	1.691	0.736	9.54(0.25)[d]	9.54(0.25)[d]	N	Mg I, Fe II
081222	2.77	0.8168	0.52(0.01)	0.28(0.11)	N	Mg I, Fe II
		1.0708	1.46(0.23)	0.61(0.21)	F, L, I	Fe II
091208B	1.063	0.784	0.65(0.43)	1.03(0.43)	N	Mg I
100814A	1.44	1.1574	0.426(0.04)	0.379(0.04)	N	Mg I
100901A	1.408	1.314	1.74(0.17)[c]	1.53(0.16)[c]	N	Fe II, Mg I
100906A	1.64	0.994	0.87(0.1)	1.19(0.1)[c]	N	
110918A	0.982	0.877	2.65(0.20)	2.82(0.20)	N	Mg I, Fe II

Notes. List of identified absorbers along the lines of sight of our parent sample. The last two columns present the subsamples they are included in ("F" = Full, "I" = Independent, "H" = High resolution, "L" = Low resolution). The features identified but not included in any sample because fall in a region of the spectra where $g(z) = 0$ are marked as "N").

[a] UVES.

[b] Also see Klose et al. (2004b).

[c] Equivalent Width measurement is lightly effected by blending. EW values are derived via deblending procedure using Gaussian fit of the two lines (either the other member of the doublet or other lines) via the `IRAF splot` tool.

[d] Equivalent Width measurement is largely effected by blending. For these lines we report the total EW for the doublet.

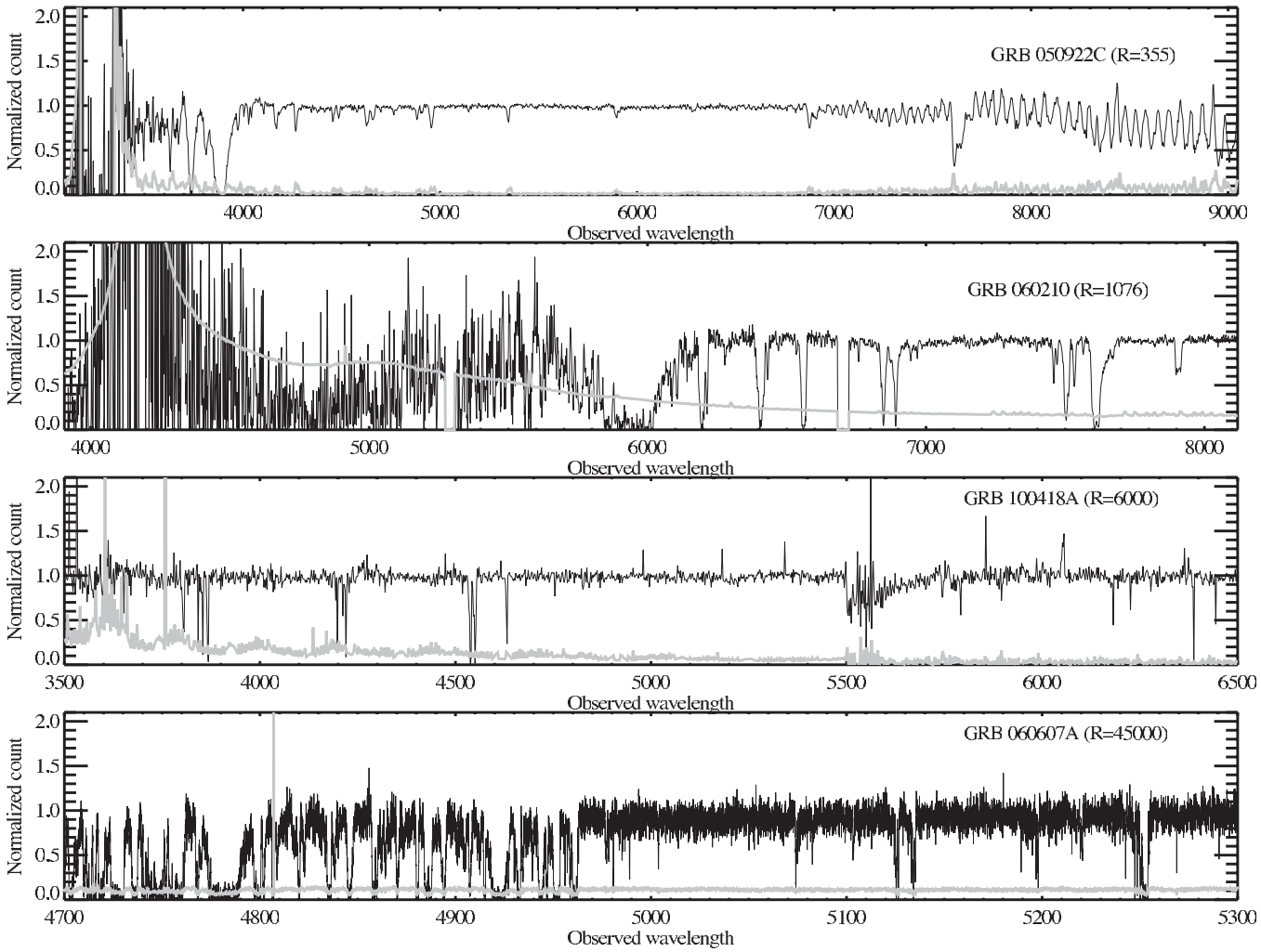

Figure 1. Comparison between four different GRB spectra obtained with different spectrographs and different resolving power. From top to bottom: GRB 050922C observed with ALFOSC; GRB 060210 observed with Gemini/GMOS; GRB 100418A observed with the UV arm of VLT/X-Shooter; section of GRB 060607A observed with VLT/UVES. In all panels, the gray curve represent the associated 1σ error spectrum.

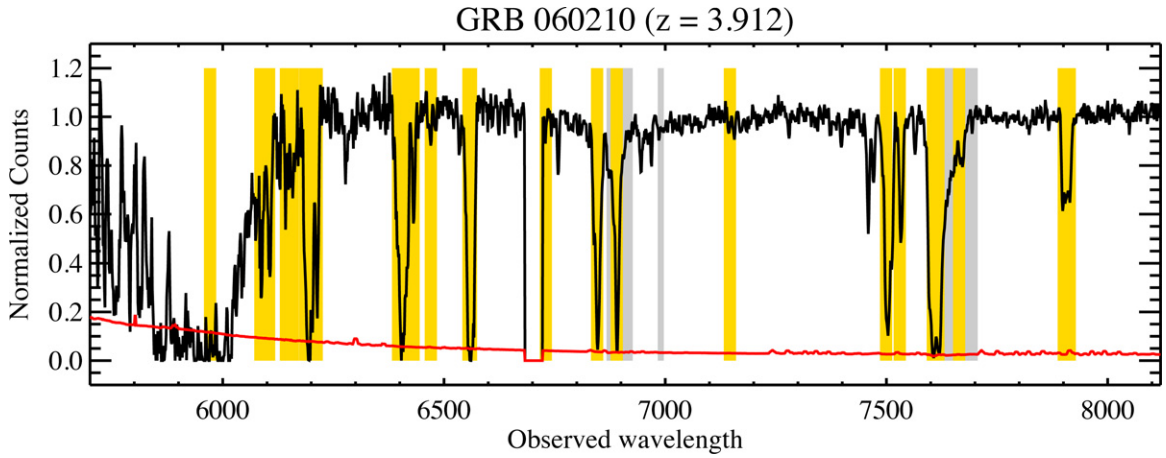

Figure 2. GRB 060210 Gemini spectrum. This example shows our excluded regions for the purpose of estimating the survey path for intervening Mg II absorption taking into account the host absorption lines (in gold, from the tabulation of Christensen et al. 2011) as well as telluric lines (in gray). The red curve is the 1σ spectrum associated with the data.

(A color version of this figure is available in the online journal.)

Many of these data were obtained by our respective research teams, although several tens were taken from public data archives or were kindly contributed by members of the community. Table 1 lists all of the sight lines with reported GRB redshifts where we were able to retrieve a spectrum. The last column lists the literature references for GRB afterglow spectra that have been previously published.

A small sample of seven GRB spectra, as mentioned in Section 1, was obtained during the pre-*Swift* era: these GRBs were discovered by non-GRB dedicated missions, like the

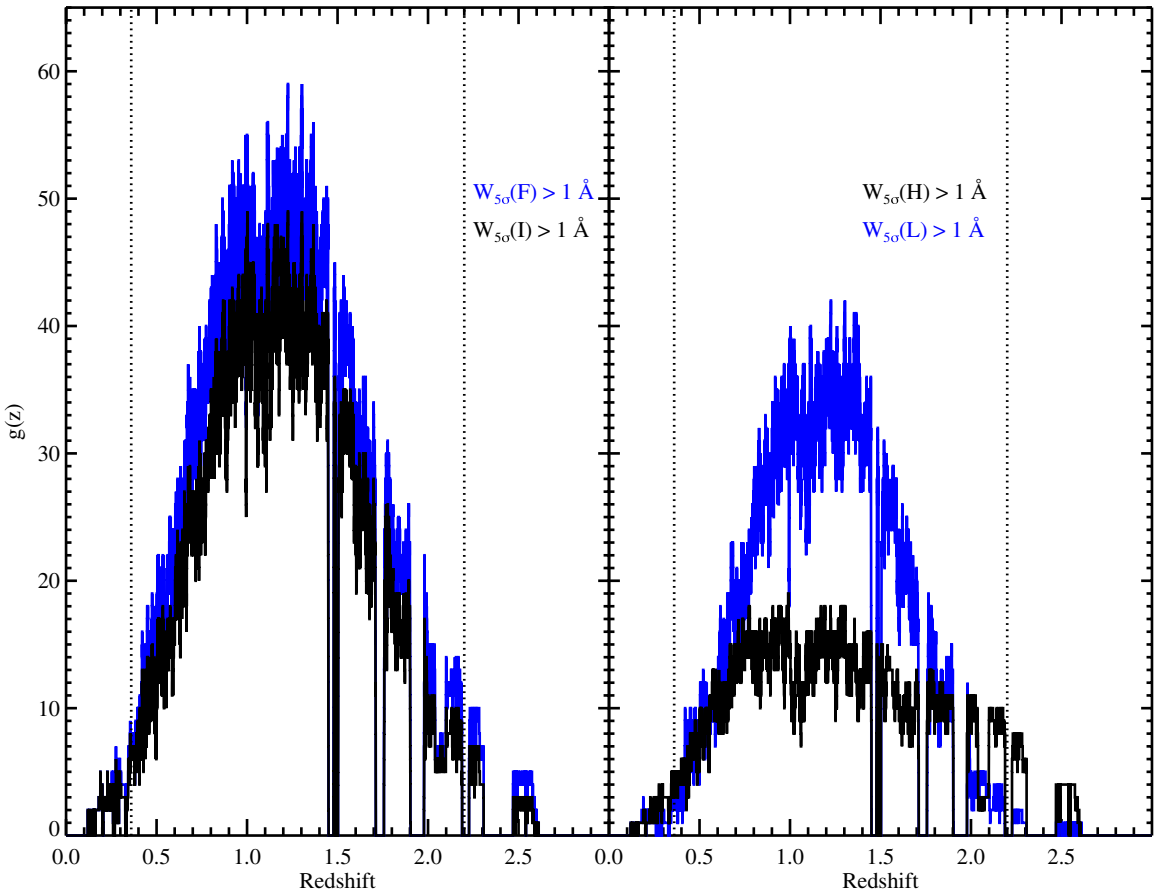

Figure 3. Left: redshift path density for 1 Å rest-frame equivalent widths at 5σ detection limit for the Sample F (blue) and Sample I (black). The dotted vertical lines represent the quasar selection regions where the Mg II doublet is detectable in the SDSS spectral coverage. Right: similar plot for Sample H and Sample L.
(A color version of this figure is available in the online journal.)

Interplanetary Network (GRB 000926), Beppo-SAX (GRB 010222), and HETE-2 (GRB 020813, GRB 021004, GRB 030226, GRB 030323, GRB 030429), and followed from the ground several hours (if not days) after the events were discovered. Nevertheless, these data have sufficiently high quality to be included in our work.

Our large data set consists of a total of 118 GRB afterglows observed by different facilities and instruments (see Table 1). The spectral resolution of these data ranges from 450 km s^{-1} (or ∼13 Å , NOT/ALFOSC) to 7 km s^{-1} (∼0.13 Å, HIRES/UVES). This large variety of data give us the opportunity to test different subsamples drawn from the overall 118 spectra. All the data presented are part of a public repository of GRB spectra.[15]

Most of the FORS1/2 data are part of the catalog presented in Fynbo et al. (2009) and de Ugarte Postigo et al. (2012), while most of the high-resolution ones (HIRES, ESI, UVES) were already published in single-GRB papers or as part of Vergani et al. (2009). A large fraction of the Gemini spectra are presented here for the first time, and are the result of our group's follow-up efforts over the last 7 yr (see also Cucchiara 2010). We encourage the readers to refer to the reference in the last column in Table 1 for the data reduction procedures and the original published papers. In the following sections, we will briefly review the reduction procedure for the Gemini and the X-Shooter data.

[15] http://grbspecdb.ucolick.org/

2.1. Gemini Sample

These data sets are part of several follow-up programs for which ToO time was awarded between 2005 and 2011. All the data included were obtained with the Gemini Multi-object spectrographs (GMOS; Hook et al. 2004). The typical observation sequence consists of two spectra in two dithered positions along the slit (usually 1″ wide) in order to facilitate sky-line subtraction. Immediately before or after the science frames, a ThAr lamp is observed and a flat field is obtained in order to allow data reduction "on the fly."

We used the `GEMINI/GMOS` data analysis packages under the IRAF[16] environment in order to perform the basic reduction, flat fielding, and wavelength calibration. Cosmic rays were identified and replaced by a median of the surrounding pixels which were not flagged as bad pixels. For this purpose we used the `lacos_spec` tool (van Dokkum 2001). Finally, one frame was subtracted from the other to remove the strongest skylines. This procedure provides good results at $\lambda < 8000$ Å, but leaves significant residuals in the reddest portion of the spectra where the GMOS spectrographs suffer substantial CCD-fringing. Therefore, the extracted error arrays associated with the Gemini-GMOS data reflect these higher-noise patterns at longer wavelengths.

[16] IRAF is distributed by the National Optical Astronomy Observatory, which is operated by the Association for Research in Astronomy, Inc., under cooperative agreement with the National Science Foundation.

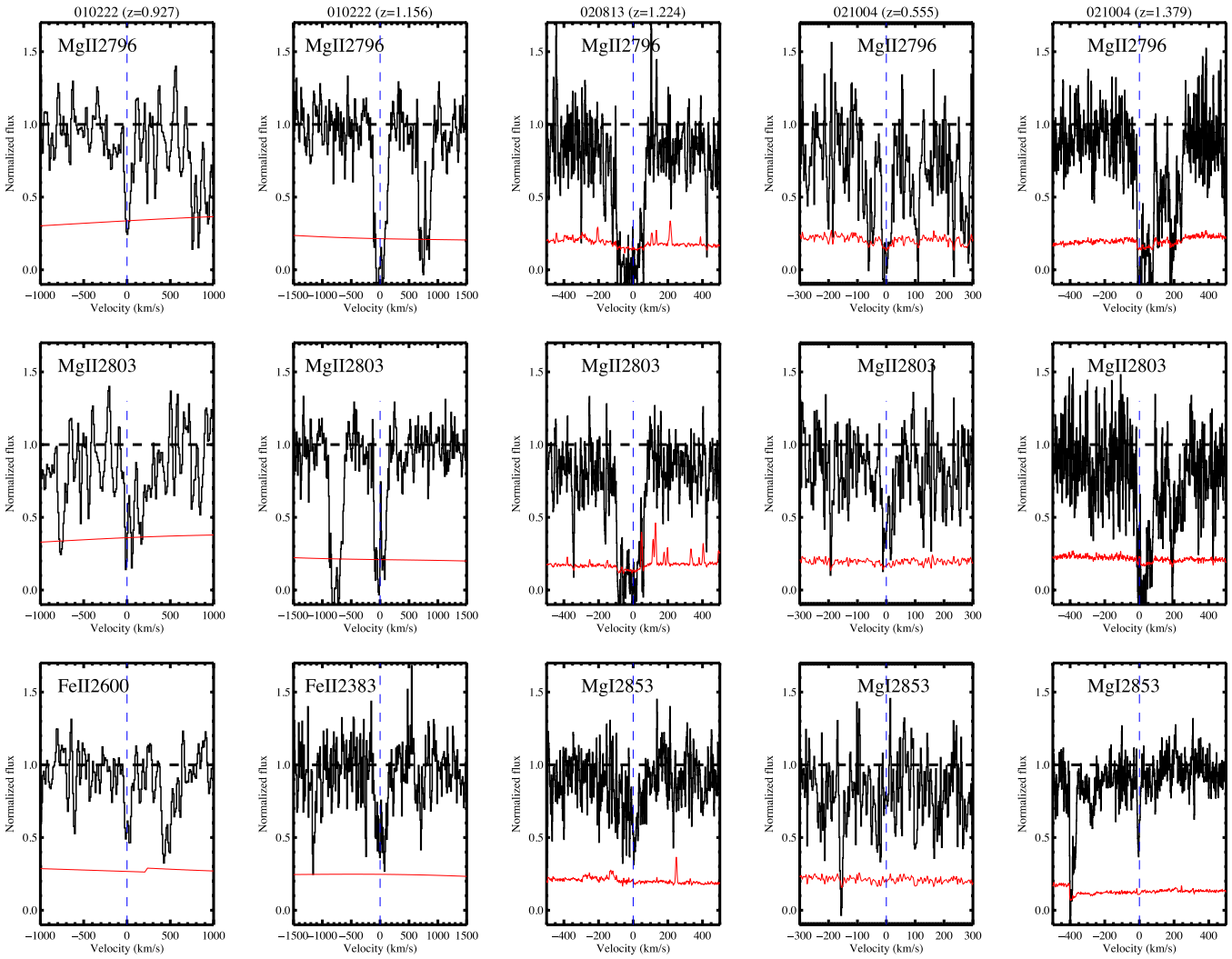

(a)

Figure 4. Line profiles of strong Mg II transitions along GRB sight lines.
(A color version of this figure is available in the online journal.)

One-dimensional spectra were then extracted using the IRAF `APALL` tool and co-added weighting each spectrum by the inverse of its variance spectrum in order to increase the S/N of the final result. The `APALL` package also produces a one-dimensional array with the poissonian statistical error and the one-dimensional sky background (estimated in regions selected far from the object trace, so to avoid any spurious contamination). These last two arrays have been summed in quadrature to obtain the final error array per pixel. In some cases, we assess the quality of the extracted error array with the estimated rms of the data array and modified the latter in order to fully account for the poissonian fluctuations in the actual data. Finally, using the `splot` routine we estimated S/N over the whole wavelength range (also reported in Table 1).

2.2. X-Shooter Data

Data for GRB 090926A and GRB 100418A were obtained via the ESO Archive[17] and reduced with version 1.3.7 of the X-Shooter pipeline (Goldoni et al. 2006) in physical mode. The spectra in the UVB and VIS arms were used for the redshift path-length estimate as well as the Mg II search. We do not use the NIR arm due to the high level of contamination from skylines in the infrared. Furthermore, the infrared sample of QSO spectra, largely obtained by Matejek & Simcoe (2012), are still small compared to the large compilation from SDSS.

2.3. Subsamples

The set of spectra listed in Table 1 comprises our full sample for analysis which we refer to as Sample F. This sample maximizes the survey path for Mg II absorption along GRB sight lines. From this parent sample, we consider several subsamples for the same analysis. Most important is the independent subsample (Sample I) which ignores all of the data analyzed in the original paper of P06. We focus first and foremost on this subsample to perform a complementary study. In addition, we consider two other subsamples which cut the data according to spectral resolution: we combined all the high-resolution spectra, obtained with echelle or echellette spectrographs (ESI, HIRES, MagE, and UVES) in Sample H and all other data in Sample L. These are summarized in Table 2.

[17] Based on observations made with ESO Telescopes at the La Silla Paranal Observatory under program IDs 60.A-9427(A) and 085.A-0009(B).

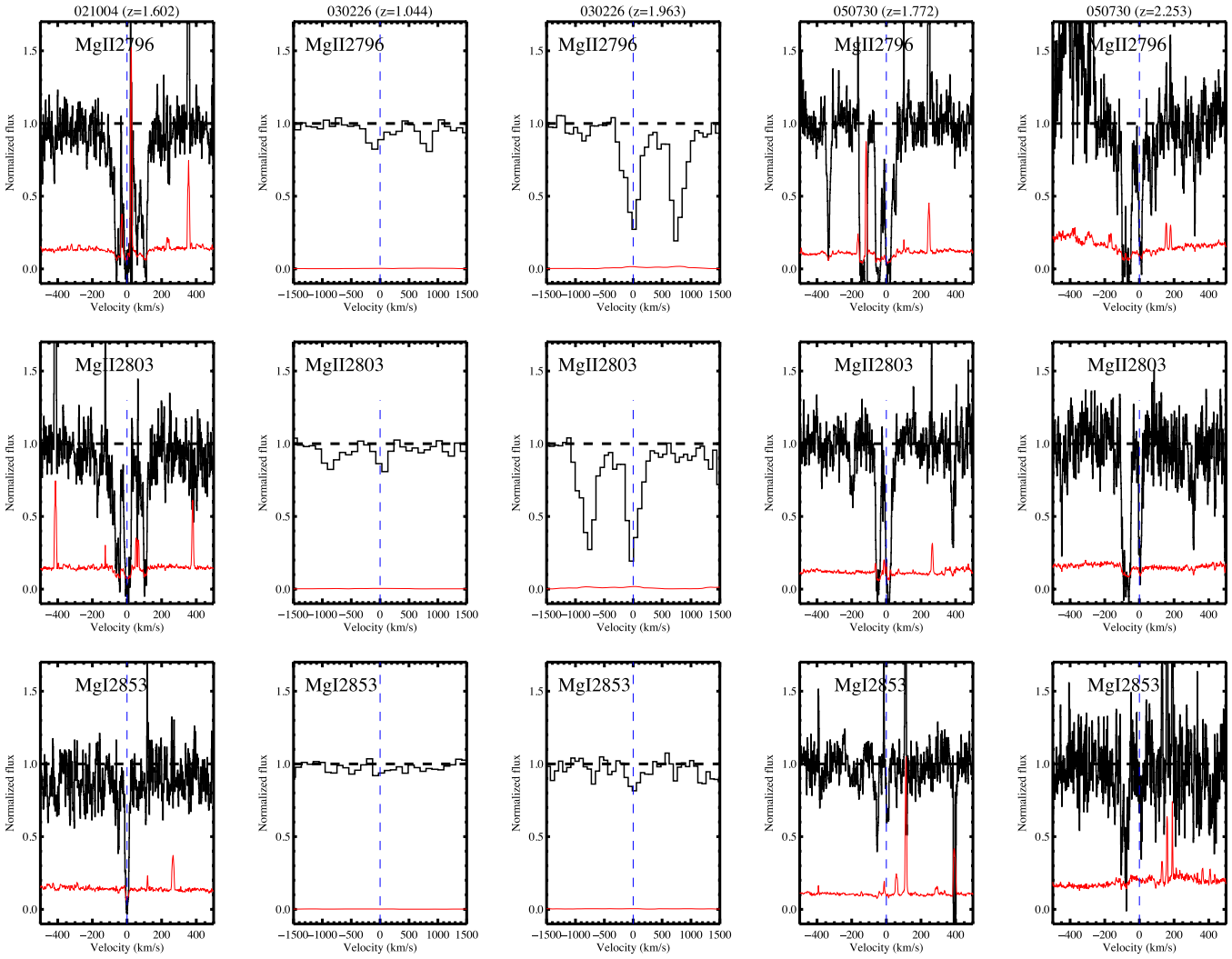

(b)

Figure 4. (Continued)

3. SURVEY PATH

The starting point of a survey for intervening absorption-line systems is to estimate the redshift path density $g(z)$. This function expresses, as a function of redshift, the number of unique sight lines for which an absorption line could be detected in the survey to a limiting equivalent width. In practice, one determines for each spectrum those regions that have sufficient S/N and are free of strong blending by terrestrial or intrinsic gas. These specific windows define redshift intervals j, $[z_1^i, z_2^i]_j$, for the ith quasar (or GRBs) where $g(z) = 1$ within each window and zero otherwise. By integrating $g(z)$ across the full spectrum, one recovers the redshift path Δz_i covered by the source.

To properly determine $g(z)$ for each sight line, several issues must be considered to minimize systematic effects that could bias the search. First, we exclude from the search the wavelengths (or the redshift ranges) that fall in the atmospheric telluric bands, which heavily absorb the afterglow flux, rendering it very difficult to identify any features (intrinsic to the GRB, or QSO, host or intervening). Since some of our spectra extend toward the near-IR regime, we also consider atmospheric absorption at these wavelengths. A complete list of the excluded regions is presented in Table 3.

Second, GRB afterglow spectra exhibit strong absorption lines belonging to ionic species located in the progenitor environment and up to tens kpc along the line of sight. The number of detected host features varies depending on the brightness of the afterglow, the properties of the host galaxy, the S/N, and the resolution of the spectrograph (see Figure 1). Christensen et al. (2011) created a high-S/N composite spectrum using 66 afterglow spectra obtained with low- and mid-resolution spectrographs. Strong absorption lines were identified as well as weak ones previously undetected in the individual spectra. Since most of these lines are common in GRB host galaxies we compile a sublist of these absorption features to be excluded in our redshift path-length calculation. We included also some of the most common fine-structure transitions. To be more conservative, a region equivalent to one-half resolution element both blueward and redward of the observed central wavelength of the considered transition (as set by the redshift of the host galaxy) has had $g(z)$ set to zero. This choice has only a minor effect on the total redshift path covered, since the amount of path lost is of the order of 1%–2%. In the cases of high-resolution spectra, the minimum size of the masked region is 200 km s^{-1}. A complete list of these features is also presented in Table 3.

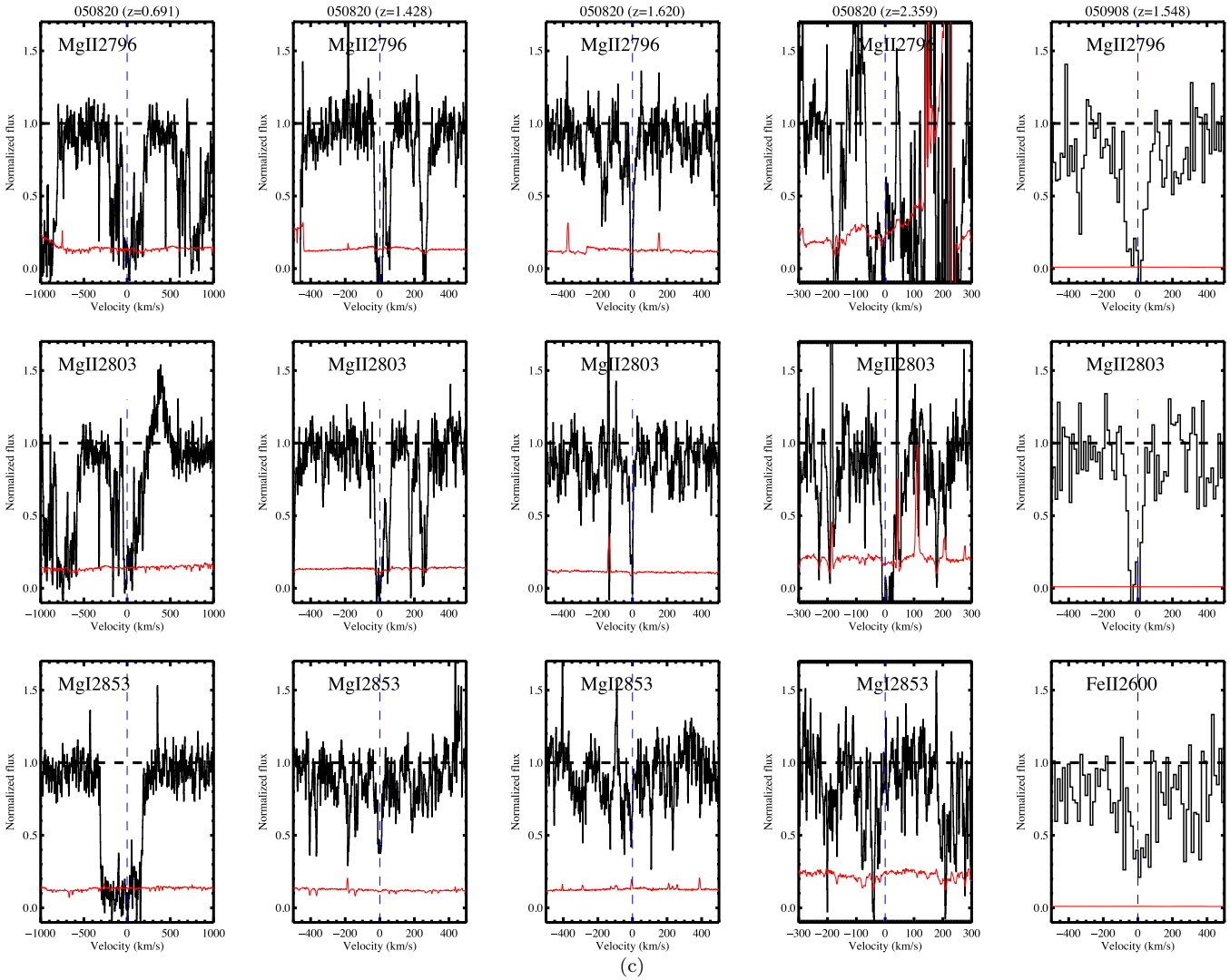

(c)

Figure 4. (Continued)

Finally, for some of the spectrographs (e.g., UVES, GMOS), the spectral coverage is non-contiguous due to gaps between detector chips and/or the use of multiple cameras. Regions without data were simply masked in the $g(z)$ evaluation. In several cases, regions beyond ∼8000 Å were heavily effected by fringing, even after correcting for it in the data processing. We opted for a visual inspection of the data and decided on a case-by-case basis which regions needed to be excluded for the search. As an example, in Figure 2 we present the Gemini/GMOS spectrum of GRB 060210, where all of the masked regions are indicated. It is clear from Figure 2 that the maximum redshift, $z_{\rm max}$, allowed for our intervening Mg II search is dictated by the host galaxy redshift, in particular, we begun our search starting 1500 km s^{-1} blueward the corresponding Mg II feature (or $z_{\rm max} = z_{\rm GRB} - 0.015$). Also, the minimum, $z_{\rm min}$, is indicated either by the bluest wavelength covered by the spectrograph or, as in the case of GRB 060210 where the GRB is at sufficient enough redshift, by the presence of the Lyα feature (at rest-frame $\lambda^{\rm rest}_{{\rm Ly}\alpha} = 1215.67$ Å) such that $z_{\rm min} = ((\lambda^{\rm obs}_{{\rm Ly}\alpha}/2796) - 1) + 0.05$, where $\lambda^{\rm obs}_{{\rm Ly}\alpha} = \lambda^{\rm rest}_{{\rm Ly}\alpha}(1 + z_{\rm GRB})$ (or equivalently ∼5000 km s^{-1} redward the Lyα feature). We do not extend the search for intervening Mg II into the Lyα forest and we avoid the (typically) very strong damped Lyα absorption profile of the GRB host galaxy.

Once these regions have been excluded, we determined the 5σ equivalent width limit per pixel using the following procedure: an ideal absorption line would be broadened, among other effects (like thermal broadening), by instrumental effect due to the spectrograph characteristics, producing broader profiles (e.g., Gaussian shape) at low resolution and narrower at high resolution. It is clear that our capability to distinguish a "true" feature from noise fluctuations, and to measure accurately its equivalent width, strongly depends on the S/N of the spectrum. We constructed an equivalent width limit "spectrum" using the formalism introduced by Horne (1986) in a similar fashion as in Schneider et al. (1993): using the data variance spectrum to each pixel we estimated the 1σ equivalent width limit performing a weighted sum of the variance values using as weights a normalized Gaussian centered at each pixel and having width set by the resolution of the spectrograph (FWHM $= S \times 2.35$, where S is the spectral resolution element).

Finally, at each unmasked pixel in the spectrum, we query whether a 5σ equivalent width limit is below a given rest-frame minimum equivalent width value for Mg II 2796 (e.g., in our case 1 Å). If this condition is satisfied, we query whether the corresponding Mg II 2803 line lies in an unmasked region. If both of these criteria are satisfied, $g(z) = 1$ at the redshift corresponding to that pixel otherwise we set $g(z) = 0$. This

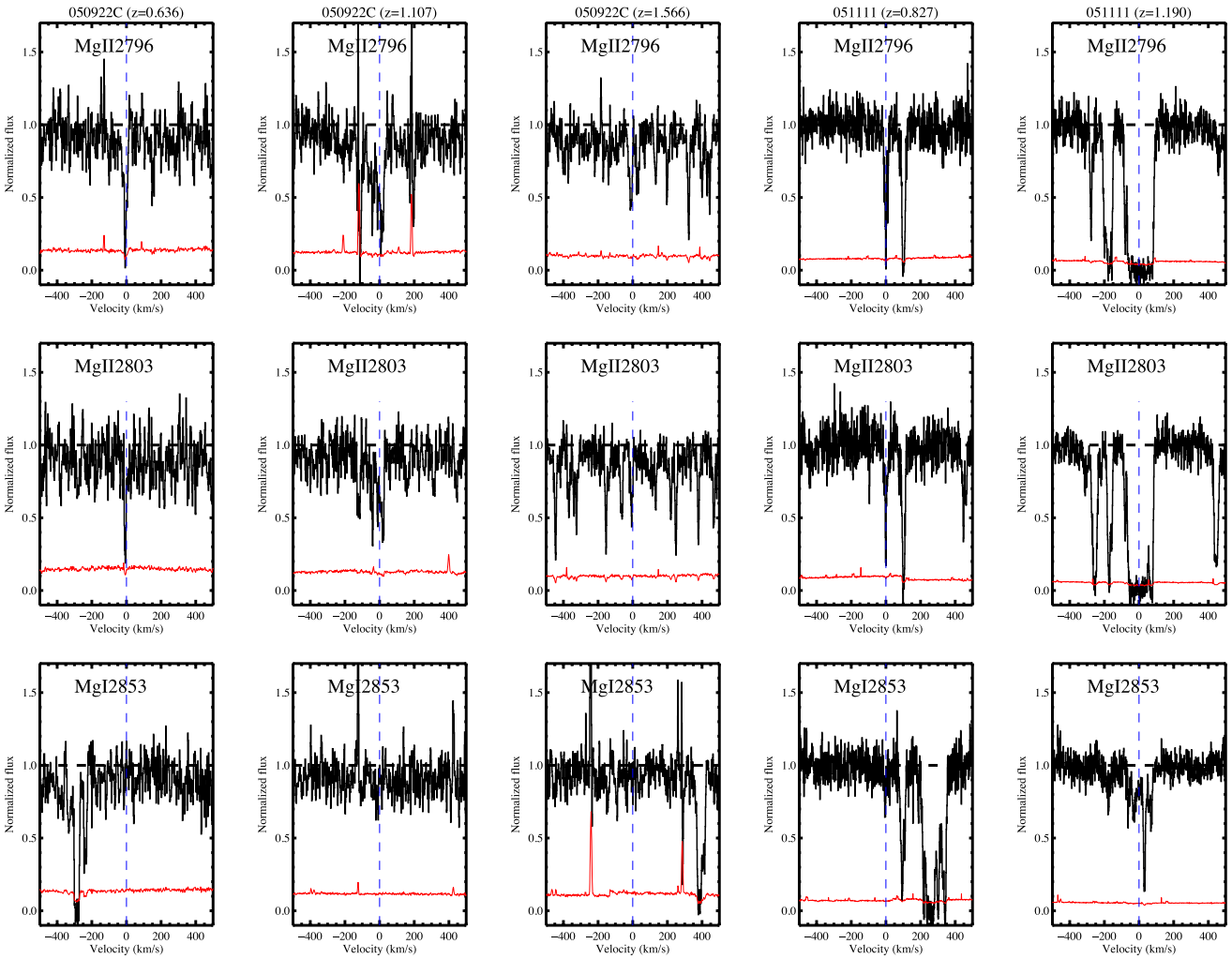

(d)

Figure 4. (Continued)

generally leads to a series of discontinuous redshift intervals for the Mg II survey, as listed, for example, in Table 4 for GRB 030226.

Figure 3 presents the total redshift path density for Sample F and Sample I, which represents the number of GRB sight lines available for our Mg II search as a function of redshift. These are shown for a limiting rest-frame equivalent width of 1 Å at 5σ confidence. It is immediately clear from this figure that we accurately excluded from our analysis the telluric lines regions (i.e., at $z_{\rm Mg\,II} \sim 1.5, 1.7, 1.9$, and 2.4). Also, the analysis is mainly performed where we have the majority of the searchable path, in the $0.36 \lesssim z \lesssim 2.2$ interval range (as done in previous QSO searches as well as in P06), due to the larger statistical sample from the GRB and the QSO samples.

The total Δz of the survey crudely expresses its statistical power. This may be calculated by simply summing the Δz_i values for each source. For the full sample (F), a redshift path length of $\Delta z = 55.5$ for the 1 Å equivalent width limit. For the independent sample (I), we find $\Delta z = 44.9$. The latter represents a ~3 times larger surveyed path than P06.

4. IDENTIFYING AND MEASURING INTERVENING Mg II ABSORBERS

We described in the previous section the construction of the redshift path density which defines, for each spectrum, the regions where an intervening Mg II doublet may be detected at 5σ significance. Independent of this calculation, we have searched each sight line for the presence of Mg II absorbers using an automatic procedure: from the constructed equivalent width spectrum (see previous section), we determined every feature satisfying a 5σ detection threshold via an automatic procedure similar to the C IV doublet search performed in Cooksey et al. (2010). We considered each line as a possible Mg II absorber, and confirmed this association through the presence of a proper Mg II doublet (both in velocity separation and relative W_r). Finally, we inspected every candidate identified by this procedure visually, confirming the presence of a genuine doublet with the additional identification of other common features (e.g., Mg I Fe II). We also accurately measured the equivalent widths of the doublet components via line profile fitting or, in the case of line-black saturated transitions (e.g., high-resolution data), by pixel summation. We also estimated the uncertainty in our W_r values by summing the pixel-by-pixel variance in quadrature (see Table 5). As sanity check, each GRB sight line was also manually inspected by the lead authors in search of Mg II doublets that might be missed by the automatic screening process. We found two doublets in addition to the candidates automatically identified which may be Mg II features (see Section 4.1 for our completeness analysis). Also, we found some doublets which were misidentified as Mg II doublets: in reality these features were host galaxy fine-structure transitions

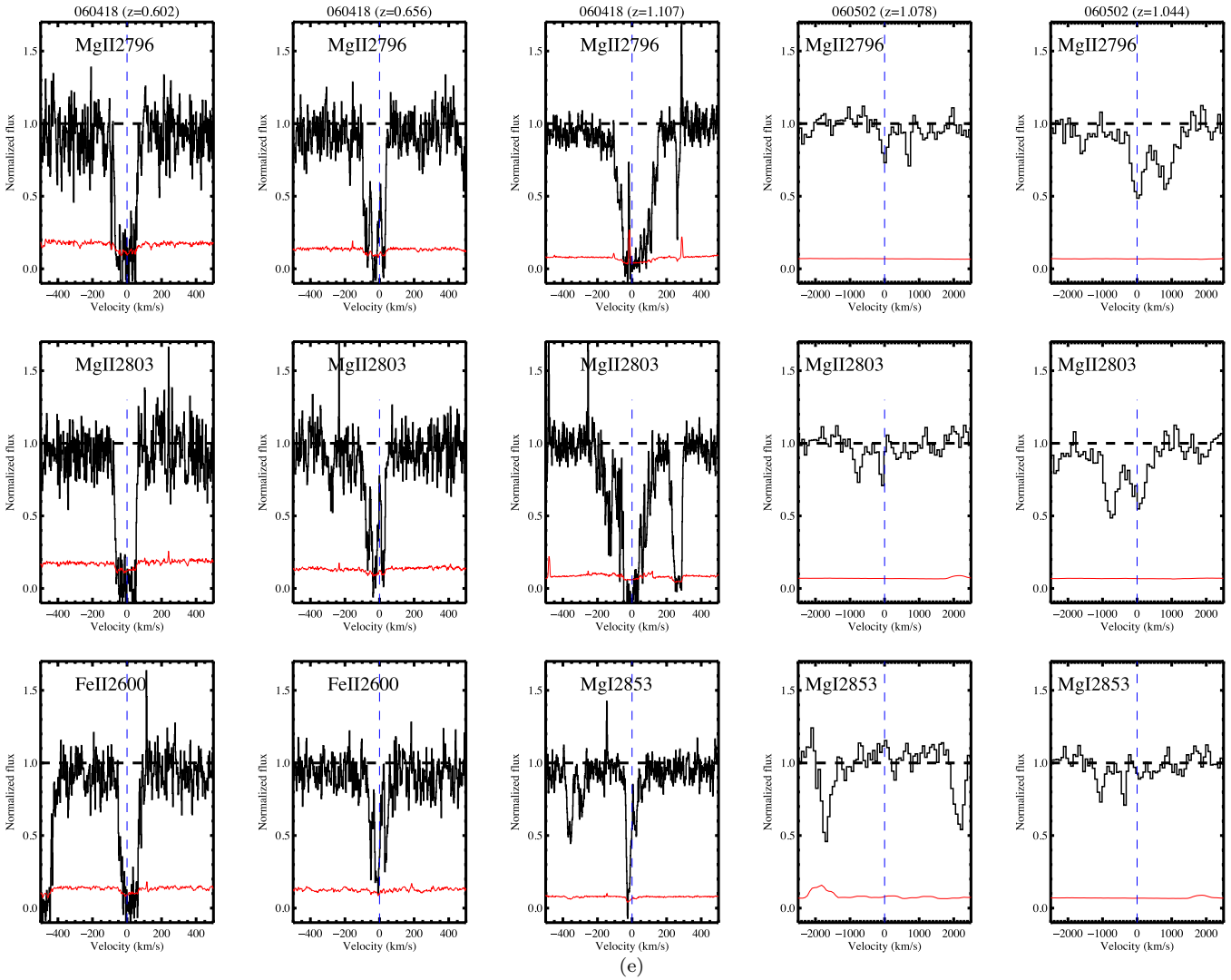

(e)

Figure 4. (Continued)

or other metal lines belonging to other intervening systems (e.g., GRB 061121). We estimated that our total redshift path length would be decreased of a factor of $\lesssim$6% if we would have masked also these features, therefore we prefer not to exclude these spectral regions to preserve a maximum searchable path. Again, our visual inspection prevent these features to be accounted in our Mg II search.

Table 5 lists the Mg II systems that have been discovered, and Figures 4(a)–(m) show the line profiles of all the strong Mg II systems in combination, when available, with other metal features.

4.1. Completeness Estimate

It is important to note that the sample under consideration has been obtained by a large variety of facilities and, also, GRBs have been observed at different epochs (meaning at different afterglow brightness) as well as with different atmospheric conditions. Therefore, it is worthwhile evaluating our completeness in finding very strong Mg II absorbers at the considered 5σ confidence level. To assess our completeness, we inserted mock Mg II features into our spectra (taking into account the S/N and the resolution of the original spectra) and then we reprocess these new data sets via our automatic procedure. The injected features have random equivalent widths between 0.05 and 3 Å and a maximum number of seven subcomponents, each with a range of doppler parameters b = 5–20 km s^{-1}. These features were inserted between $z_{\rm min}$ and $z_{\rm max}$ as defined in Section 3 per each GRB. We repeated this process 50 times per sight line for a total of 5250 iterations. We compared the number of injected strong features ($W_r \geqslant 1$ Å) that should be automatically identified because they were located in regions of the spectra were $g(z) = 1$ (accordingly to Section 3) with the actual recovered list: we conclude that ≈98% of the systems were correctly identified and detected as genuine strong Mg II doublets.

Figure 5 presents the equivalent width distributions of the injected and recovered features. In the top panel, the injected features (in black) are compared with the number of recovered features in the low-resolution spectra sample (L) with resolving power of $R < 600$ (dotted red line) and $R \geqslant 600$ (dashed red line) as well as the total number (solid red line): it is important to note that at rest-frame $W_r < 1$ Å the very low resolution spectrographs are unable to recover such mock features, while at $W_r \geqslant 1$ Å there is no such clear difference, strengthening our completeness result.

In the middle panel of Figure 5 we present similar comparison for the high (H) resolution sample, this time comparing only the injected distribution and the recovered one (in red). A Kolmogorov–Smirnov (K-S) test of the two distributions (total

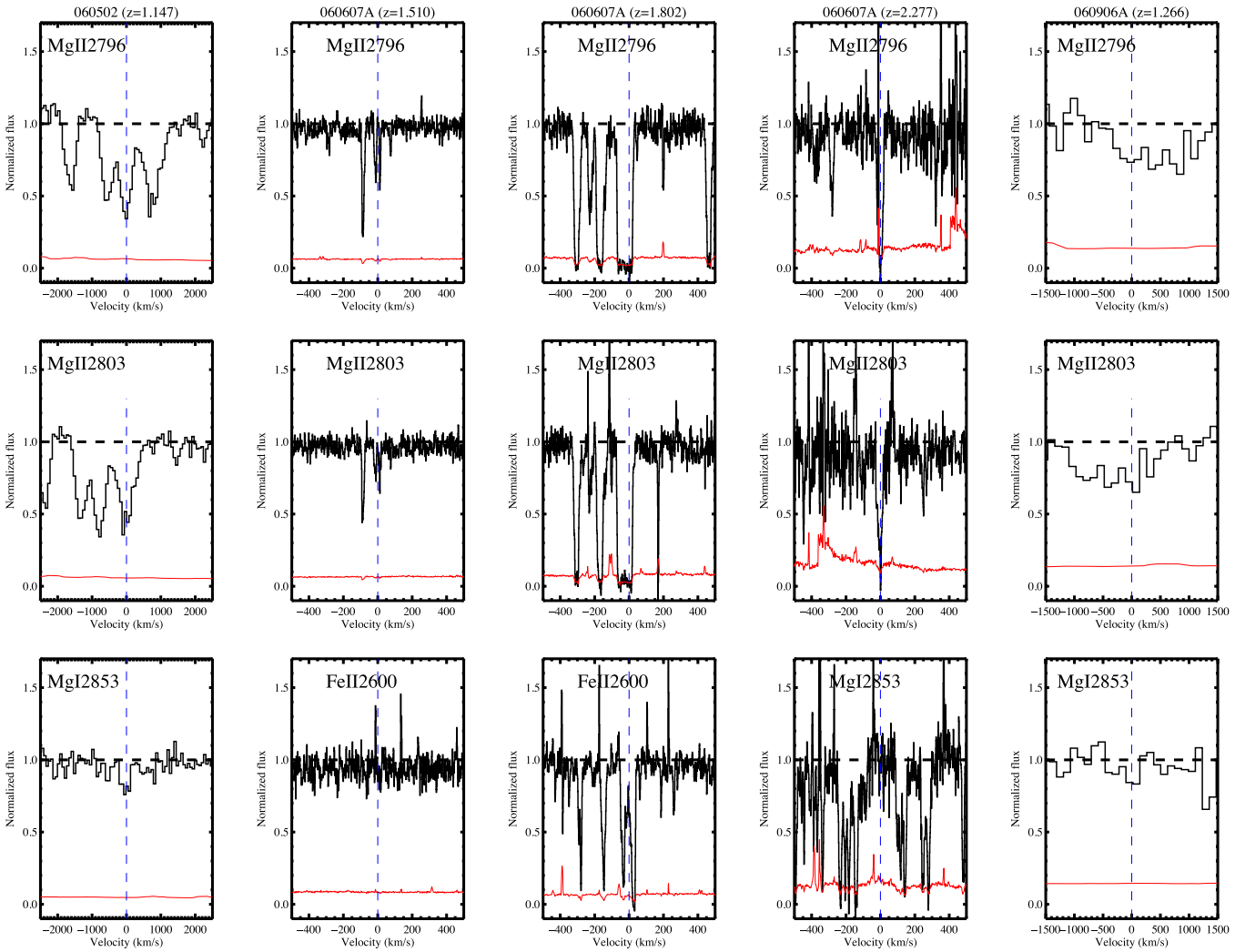

(f)

Figure 4. (Continued)

injected and total recovered in the Sample L and Sample H) shows a $\gtrsim$36% probability that they are drawn by the same parent population. It is worth mentioning again that while at $W_r \leqslant 1$ Å some features are not retrieved, as expected due to the low resolution and the noise of the spectra, some of the retrieved ones might be detected because at high redshift, boosting their observed equivalent width by a $(1 + z_{\rm abs})$ factor.

Also, most of the missed absorbers (even at $W_r \geqslant 1$ Å) in the lowest-resolution data are usually self-blended (resembling a single broad line) or they are blended with the profile wings of other lines (intervening systems metal lines or host galaxy features) preventing the automatic identification of both doublet components.

We examined again our original sample and we confidently retrieved only two such cases: GRB 090812 and a possible absorber at $z = 1.055$ and GRB 070110 with a possible doublet at $z = 1.5875$. Nevertheless, including such features, which were not automatically recovered, does not effect our conclusions.

In the bottom panel of Figure 5, we present our cumulative completeness level with increasing resolution. We reach ∼97% level around the resolution of the Gemini-GMOS instrument (R400 grating, $R \sim 1200$), whose spectra provide the best combination of S/N and resolving power to properly identify the population of strong Mg II absorbers characterizing the GRB intervening system population.

5. RESULTS

5.1. Incidence $\ell(z)$

Combining the results from the previous two sections, we may estimate the incidence of Mg II absorption per unit redshift $\ell(z)$ (also referred to as dN/dz or dn/dz). The standard estimator for $\ell(z)$ to a limiting W_r is the observed ratio of the number of absorbers discovered, N, having $W \geqslant W_r$ in a given redshift interval $[z_1, z_2]$ to the total redshift path length searched, Δz, in that redshift interval

$$\ell(z) = \frac{N}{\Delta z} \tag{1}$$

with

$$\Delta z = \int_{z_1}^{z_2} g(z)\, dz. \tag{2}$$

Figure 6 presents our $\ell(z)$ estimates for $W_r > 1$ Å Mg II absorbers, for Sample I and Sample F restricted between

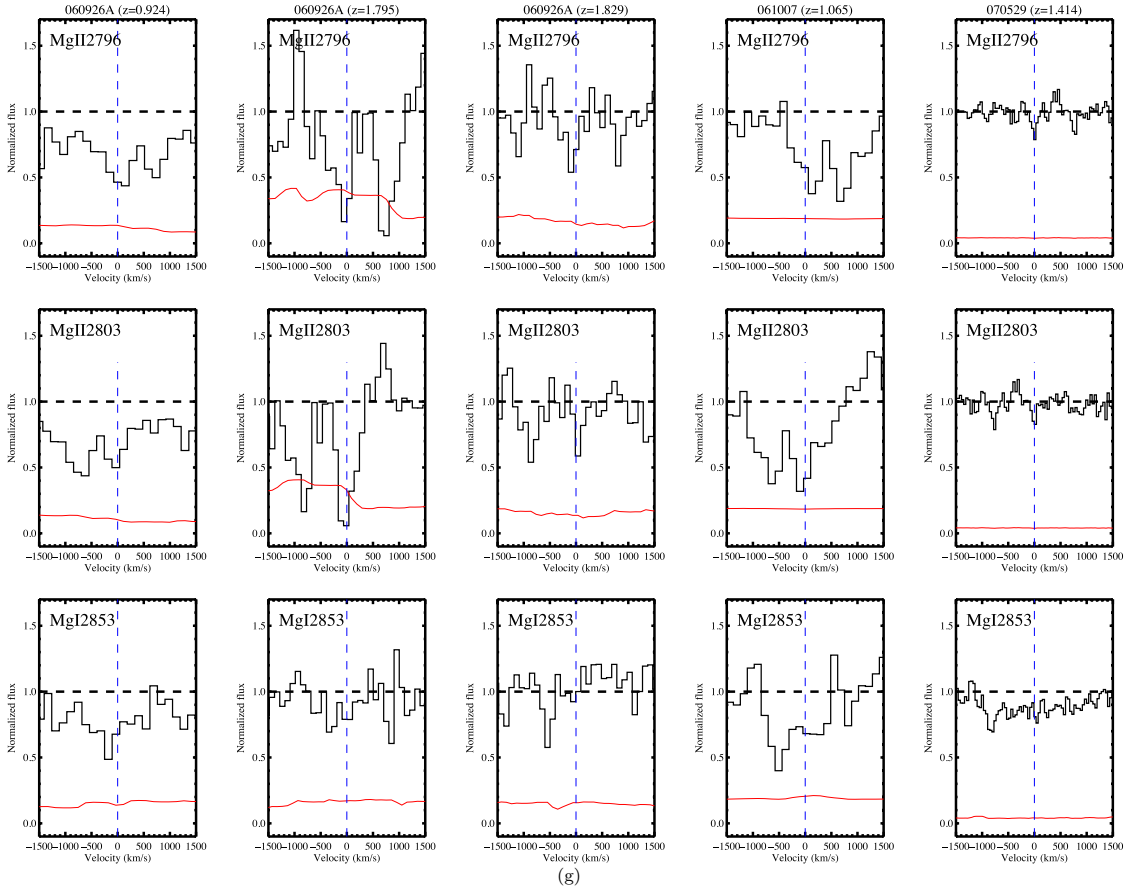

(g)

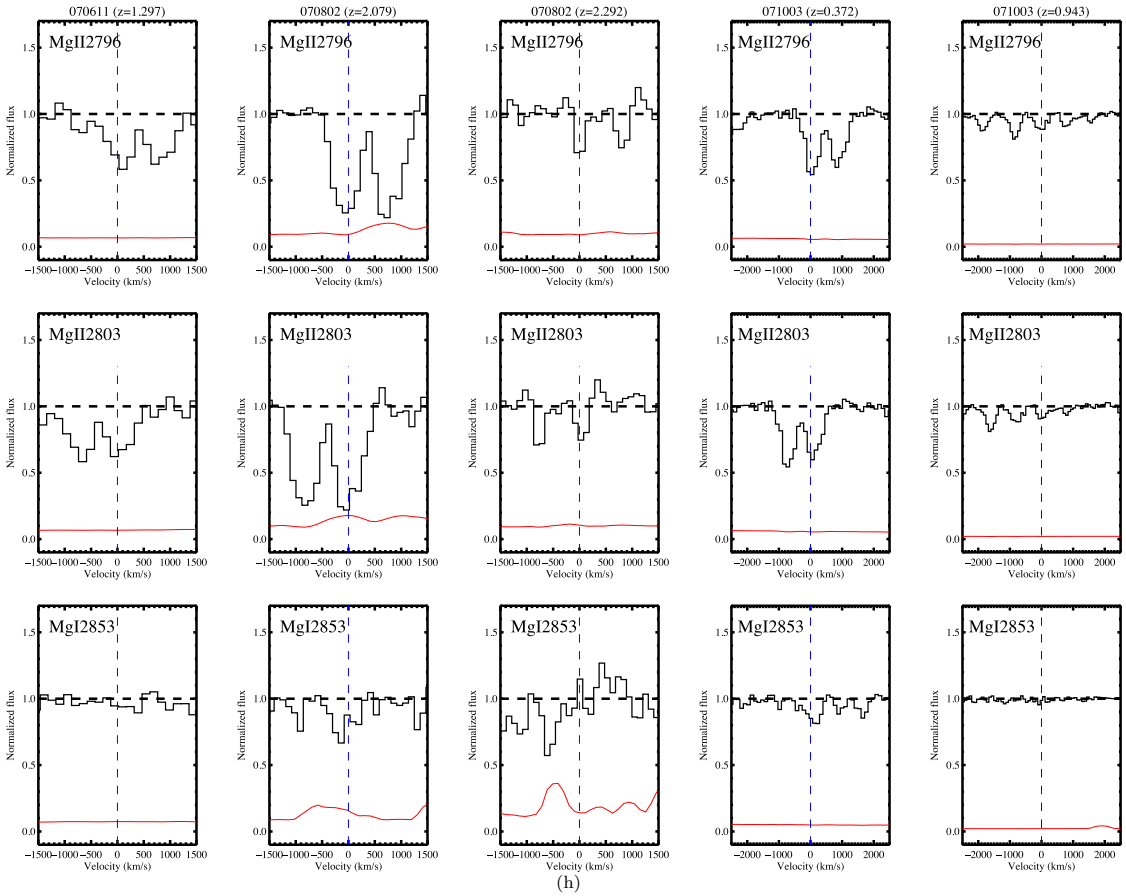

(h)

Figure 4. (Continued)

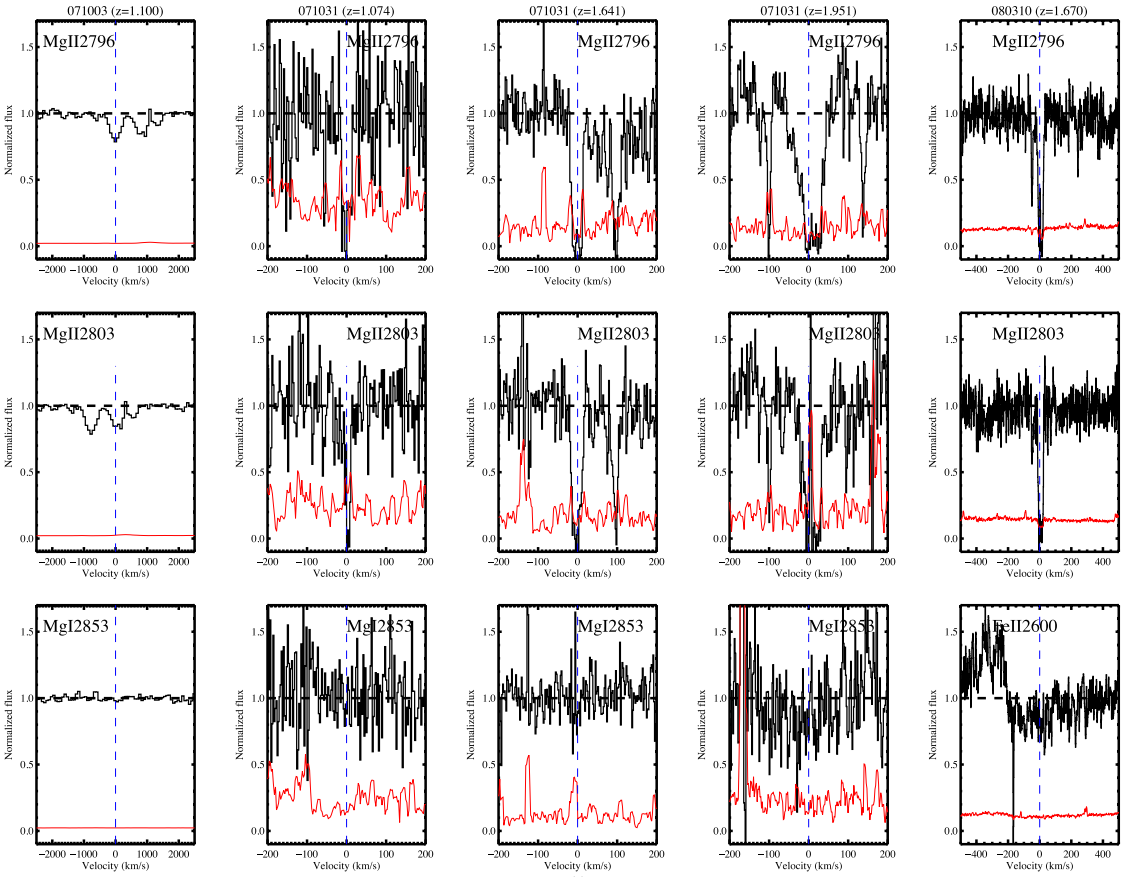

(i)

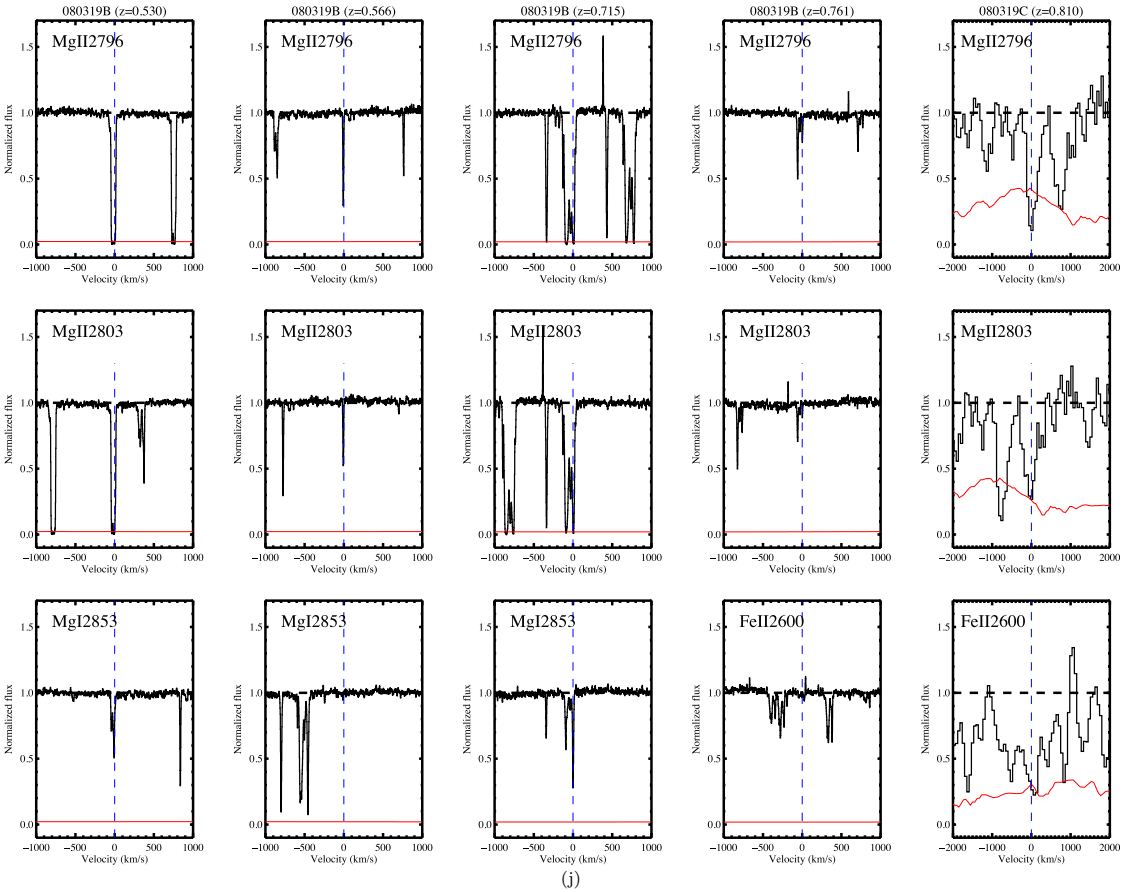

(j)

Figure 4. (Continued)

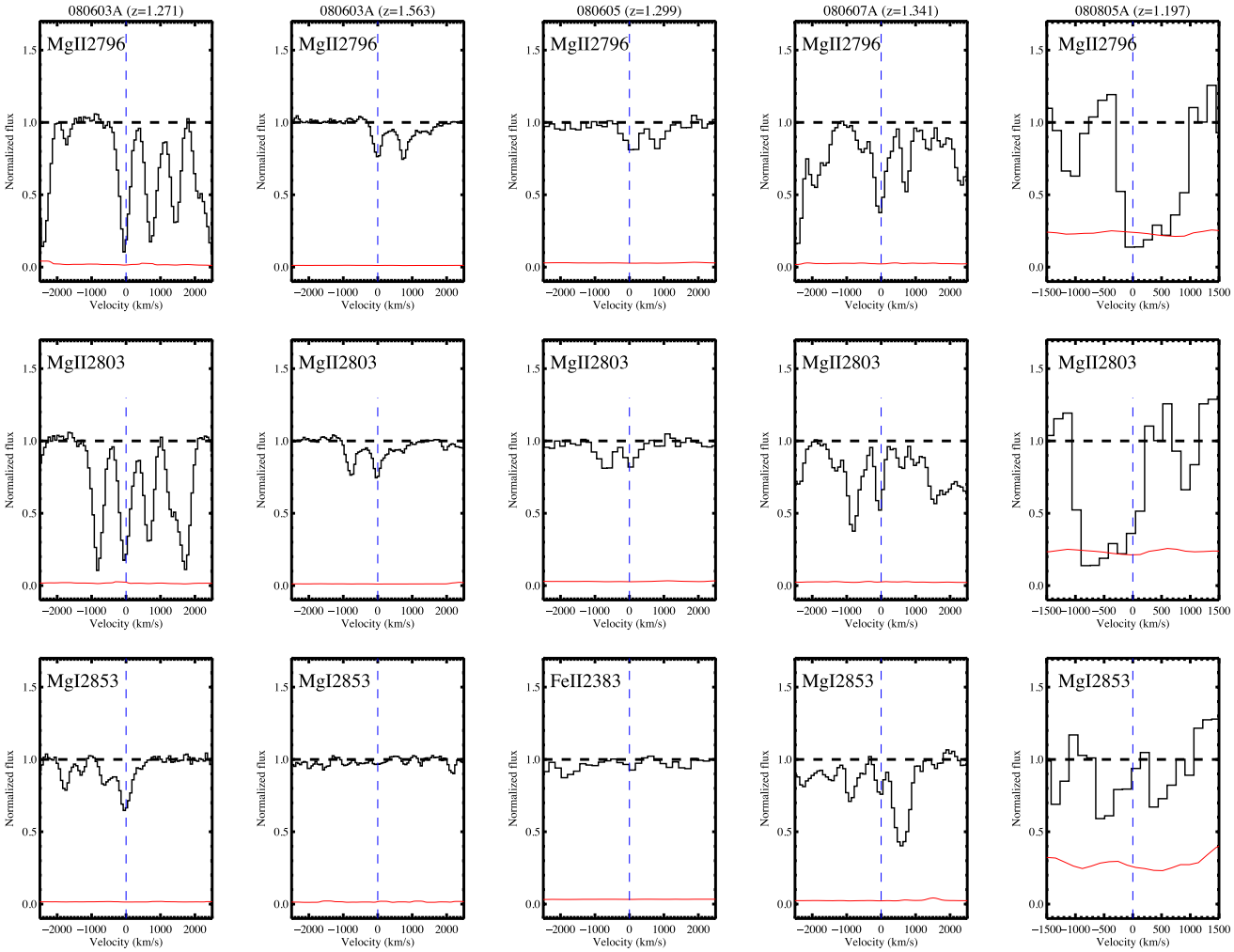

(k)

Figure 4. (Continued)

$z = 0.36$ and 2.2 The error estimates assume Poisson statistics for N and correspond to 68% confidence. The values for the GRB sight lines have roughly constant value with redshift at $\ell(z)_{\rm GRB} \approx 0.18$ and $\ell(z)_{\rm GRB} \approx 0.36$ for Sample I and Sample F, respectively.

For comparison, we display a fit to the measured $\ell(z)_{\rm QSO}$ values for $W_r \geqslant 1$ Å Mg II absorbers discovered along the thousands of quasar sight lines drawn from the SDSS (Zhu & Menard 2012). These spectra have been chosen to have S/N $\gtrsim$ 15, so to assure a high-confident statistical sample of Mg II.

This quasar sample was searched for Mg II absorbers at wavelengths redward of the strong C IV quasar line ($\lambda_{\rm rest} = 1550$ Å) and blueward of the reliable response of the Sloan fibers up to the quasar's Mg II emission line. These search criteria are substantially similar to the approach used for the GRB sample.

From Figure 6 it is evident that while the Sample I follows the expected distribution derived from the QSO analysis, Sample F still presents a modest excess of absorbers. In the case of Sample F, for instance, $\Delta z = 55.5$ and the number of absorbers identified is $N_{\rm obs} = 20$ ($N_{\rm exp} = 13$). Overall the $\ell(z)_{\rm GRB,F} = 0.36 \pm 0.09$, a factor $\sim$1.5 greater than the expected quasar density of absorbers ($\ell(z)_{\rm QSO,F} = 0.24$). Considering the independent sample, which, as mentioned in Section 2.3, excludes all the lines of sight in P06, we obtain $\ell(z)_{\rm GRB,I} = 0.18 \pm 0.06$. Following the same analysis, similar results are evident using the high-resolution and the low-resolution samples (Sample H and Sample L): in these cases we identify an overabundance of strong Mg II absorbers in the high-resolution sample, leading to a $\ell(z)_{\rm GRB,H} = 0.64$, a factor 2.6 larger then the expected ($\ell(z)_{\rm QSO,H} = 0.25$). We summarize our analysis in Table 2.

Figure 7 shows the cumulative distribution of Mg II absorbers detected from GRB Sample F and Sample I, together with the quasar estimates. We may compare these results against the predicted cumulative distribution functions for a QSO survey with identical search path to the GRB analysis by simply convolving the GRB $g(z)$ with $\ell(z)_{\rm QSO}$:

$$N^{\rm QSO}_{\rm cumul}(z > z') = \int_{0.36}^{z'} \ell(z)_{\rm QSO}\, g(z)\, dz. \qquad (3)$$

It is evident that the full Sample F exhibits a modest excess of $\sim$30%, but that the independent Sample I shows no excess. The new results for Sample I do not confirm earlier works which reported an excess of strong Mg II absorption along GRB sight lines.

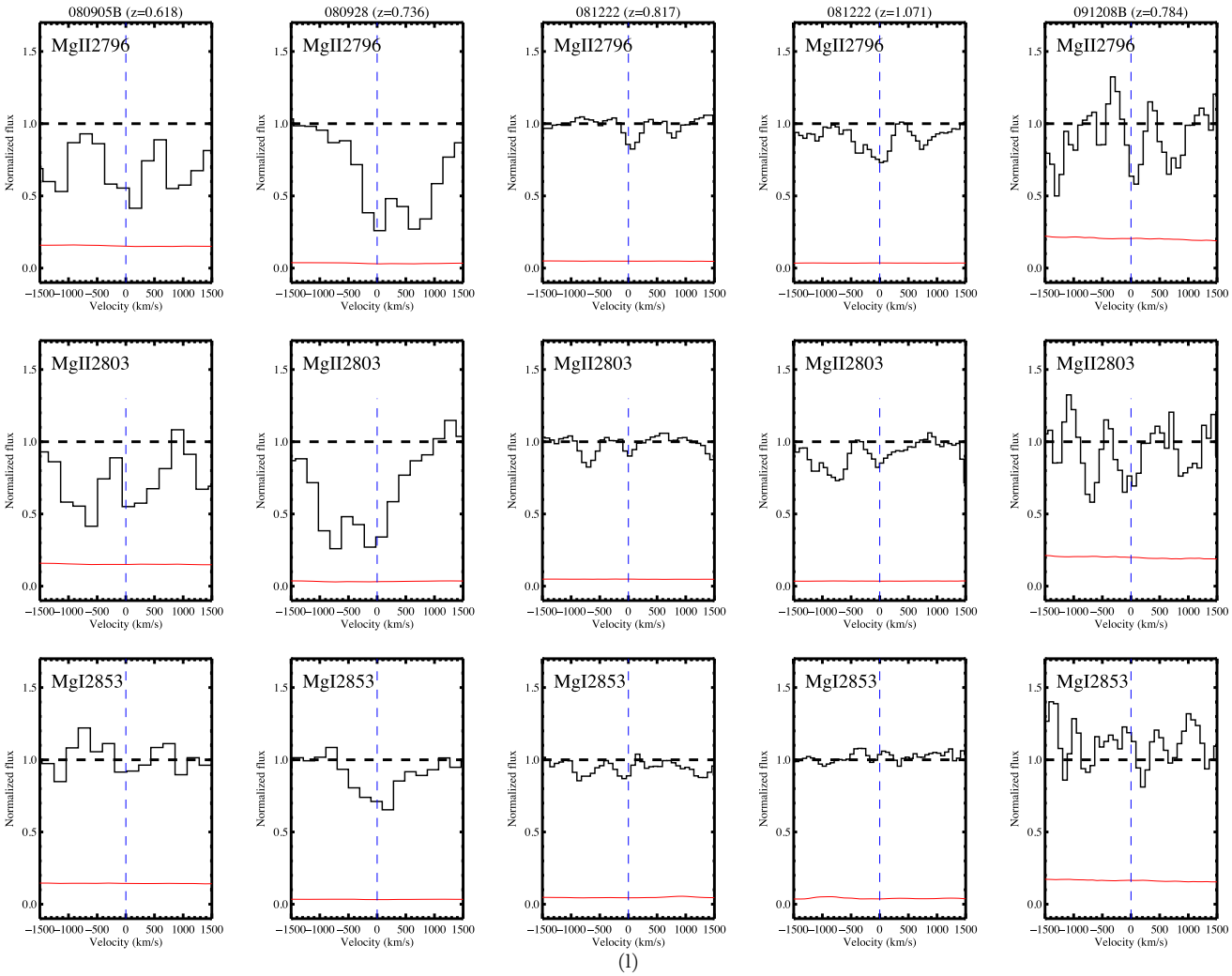

(l)

Figure 4. (Continued)

5.2. Monte Carlo Analysis

To assess the significance of these results, in particular the observed excess for Sample F, we perform a Monte Carlo analysis as follows. First, we selected a set of 12700 SDSS quasars from Zhu & Menard (2012) that have a continuous $g(z) = 1$ redshift path density from $z_{\rm min}$ to $z_{\rm max}$, where $z_{\rm min}$ is the greater of 0.36 and $(1 + z_{\rm QSO}) \times \lambda^{\rm rest}_{\rm C\,IV}/\lambda^{\rm rest}_{\rm Mg\,II}$ and $z_{\rm max} = \min[z_{\rm QSO} - 0.04, 2.2]$. This is the brighter subset of quasars in the SDSS with correspondingly higher S/N spectra. Restricting our Monte Carlo analysis to this QSO sample facilitates the generation of random samples with a survey path identical to the GRB analysis.

For GRBs with $z < 1.5$, an SDSS QSO matched in redshift will cover the survey path of the GRB analysis. For a given GRB, we selected all quasars close in redshift space to $z_{\rm GRB}$ (usually in the range $z_{\rm GRB} \leqslant z_{\rm QSO} \leqslant z_{\rm GRB} + 0.04$ there were always at least 50 such quasars). In each Monte Carlo realization, we randomly picked one and by construction adopted the $g(z)$ from the reference GRB spectrum. We then identified the total number of absorbers discovered by Zhu & Menard (2012) along the lines of sight of these quasars and recorded those that satisfy the $W_r > 1$ Å limit and have $g(z) = 1$.

For $z_{\rm GRB} > 1.5$, the Mg II survey performed by Zhu & Menard (2012) using the SDSS quasars does not extend as low in redshift as our GRB analysis because those authors truncated the search bluer then the C IV emission peak. As a result, we considered two approaches to handling this difference. The cleanest approach is to artificially truncate the GRB analysis at the same starting redshift as the quasars, i.e.,

$$z_{\rm min,GRB} = \frac{(z_{\rm QSO} + 1)\lambda_{\rm C\,IV}}{\lambda_{\rm Mg\,II}} - 1. \quad (4)$$

The other "hybrid" approach, which maximizes the survey path of this Monte Carlo comparison, is to introduce a second random quasar (with $z < 1.5$) to cover the redshift path at $z < z_{\rm min,GRB}$ in the GRB spectrum. In these cases, the minimum quasar redshift is $z_{\rm min,QSO} = (1 + z_{\rm GRB}) \times \lambda^{\rm rest}_{\rm C\,IV}/\lambda^{\rm rest}_{\rm Mg\,II} - 1$. Finally, for very high-redshift GRBs ($z_{\rm GRB} > 2.2$) the second quasar has to be chosen such that $z_{\rm min,QSO} = \min[(1+z_{\rm GRB}) \times \lambda^{\rm rest}_{\rm C\,IV}/\lambda^{\rm rest}_{\rm Mg\,II} - 1, 2]$ and $z_{\rm max,QSO} = (1 + z_{\rm GRB}) \times \lambda^{\rm rest}_{\rm Ly\alpha}/\lambda^{\rm rest}_{\rm Mg\,II} - 1$, which allows us to select at least 50 QSOs covering the desired redshift path coverage.

We ran 10,000 Monte Carlo iterations using both approaches and we recorded for each iteration the number of Mg II absorbers recovered. We performed this analysis for each of the GRB samples. Figure 8 presents our outcomes using the hybrid approach, though no relevant differences are present using the truncated redshift path.

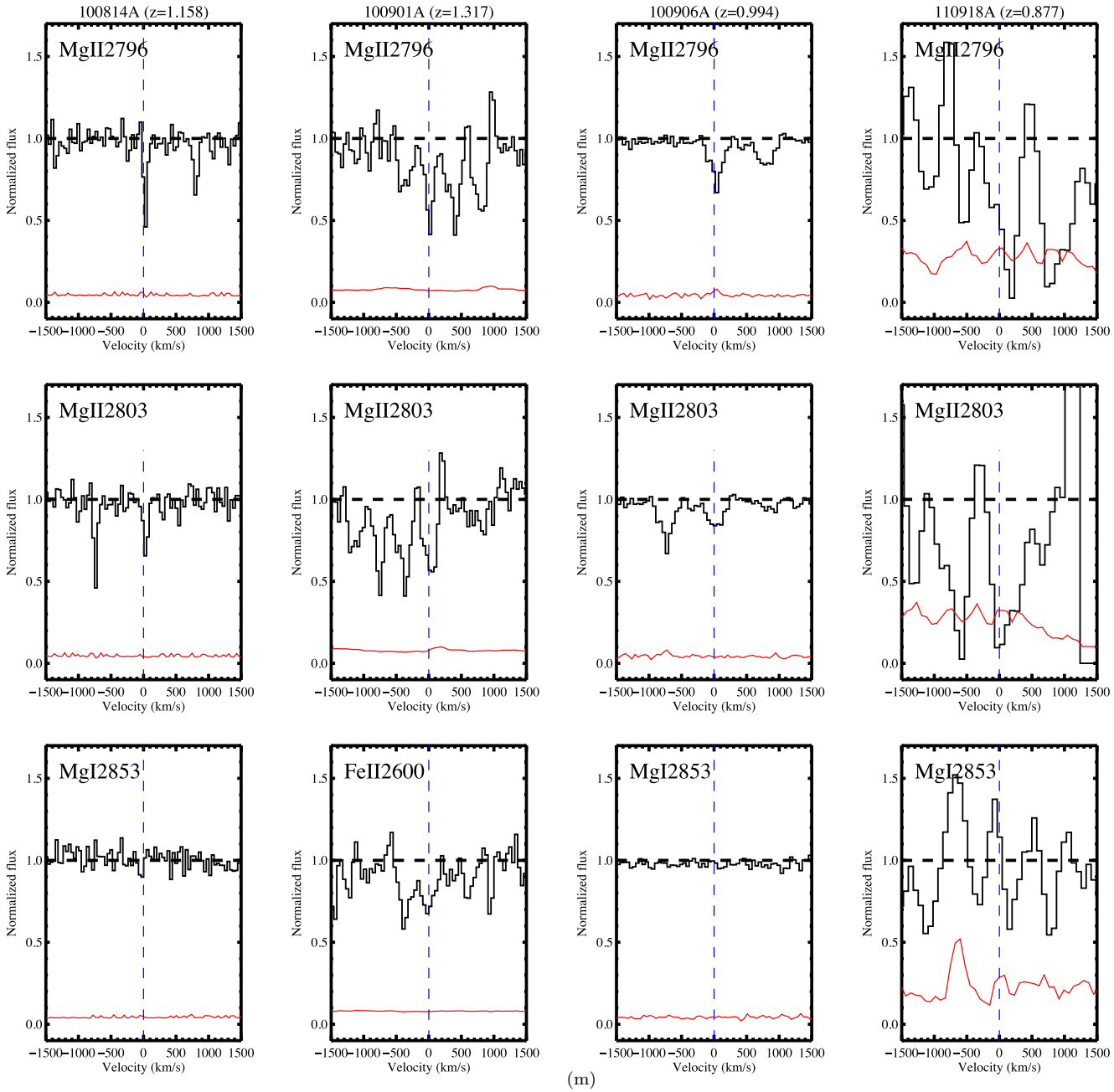

Figure 4. (Continued)

The results indicate that the incidence of Mg II absorbers detected in our independent Sample I are consistent with the results along quasar sight lines. In fact, we recovered a slightly greater number of absorbers on average along the quasar sight lines. Furthermore, the analysis shows that there is no statistically significant discrepancy between the expected total number of absorbers along the QSOs and the full parent GRB sample (Sample F). In 6% of our simulated quasar lines of sight, we observed a number of absorbers equal to or larger than the Sample F (corresponding to a 1.6σ significance). Only in the case of the high-resolution subsample, Sample H is there a statistically significant excess. This sample, however, is dominated by the sight lines analyzed in previous works (e.g., P06). We discuss this result further in the following section. A summary of our Monte Carlo analysis is given in Table 2.

It is further illuminating to estimate the statistical significance of the Mg II enhancement along GRB sight lines as a function of historical time. Figure 9 shows the results of a Monte Carlo analysis for each year, where we include all GRBs from that year and any previous. Until the end of 2006 a significant ($\gtrsim 3\sigma$) excess was present. Since that time, the statistical significance has steadily declined and the current full sample (which has several times the survey path of P06) has only a modest statistical significance. At present, we do not find a statistically significant difference in the incidence of strong Mg II absorbers between GRB and quasar sight lines.

5.3. Other Characteristics of the Mg II GRB Sample

In Figure 10, we present the cumulative distributions of the equivalent widths and relative velocities for the strong Mg II full

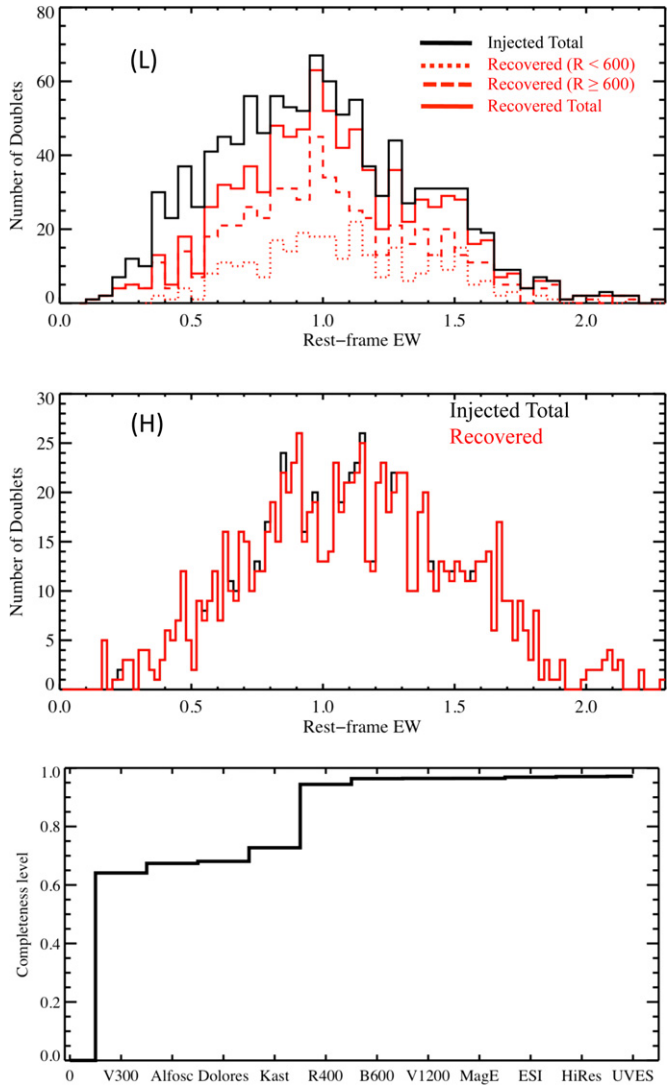

Figure 5. Top: rest-frame equivalent width distribution of the injected (black) and recovered Mg II doublets in our mock of low-resolution spectra further divided by spectrographs resolving power ($R < 600$ in dotted and $R \geqslant 600$ in dashed lines, respectively). We can see that overall, at $W_r \geqslant 1$ Å, we are able to recovered the majority of the injected features via our automatic procedure: most of the unrecovered doublets are missed or misidentified due to self-blending with other features (like other intervening systems metal lines, or wings of GRB host features). In those cases, the automatic procedure fails to identify both members of the doublet due to the low resolution of the instruments. The solid red line is the total recovered distribution. Center: same as the top panel but for the high-resolution spectra (this time we plot in red the total recovered features). In this case, we were able to retrieve almost all the injected features. Bottom: completeness level ordered by spectral resolution. From our mock sample we derived a final completeness level of ∼98%.

(A color version of this figure is available in the online journal.)

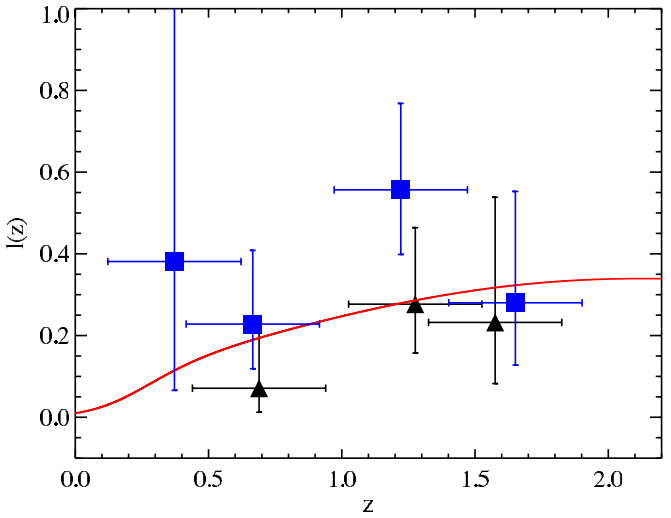

Figure 6. $\ell(z)$ evolution of intervening Mg II absorbers ($W_{2796} \geqslant 1$ Å) for our sample of GRB sight lines: triangles and square symbols refer to the Sample I and Sample F, respectively. The red curve shows the evolution of the Mg II incidence along quasar sight lines as recently computed by Zhu & Menard (2012). We derive an average $\ell(z) = 0.20$ for Sample I, in agreement with the prediction, while $\ell(z) = 0.36$ for Sample F, indicating a slight overabundance of absorbers compared to the QSOs.

(A color version of this figure is available in the online journal.)

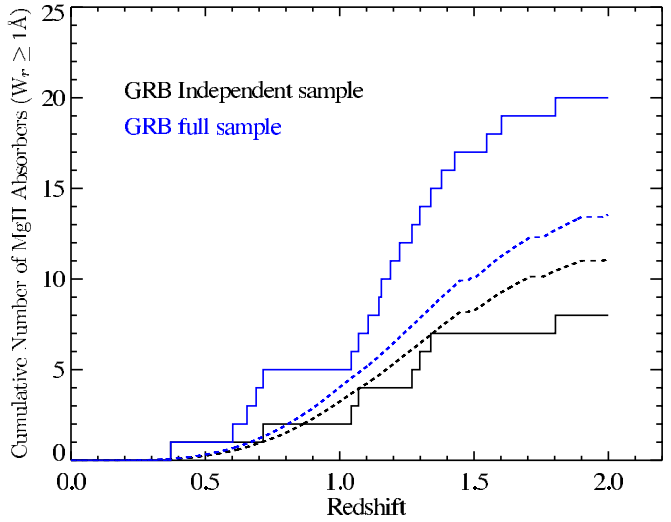

Figure 7. Cumulative distribution of strong Mg II absorbers along GRB sight lines for Sample I and Sample F (black and blue solid curves, respectively). These are compared to the predicted incidence based on measurement along QSO lines of sight (dashed curves). The independent Sample I actually shows fewer absorbers than expected while a modest excess remains in Sample F. Neither result corresponds to a statistically significant difference from the QSO results.

(A color version of this figure is available in the online journal.)

sample. The latter is calculated assuming that these intervening systems are local to the GRB environments and are moving at such velocity toward the observer to mimic a lower redshift system (see also Cucchiara et al. 2009; Vergani et al. 2009 for the intrinsic properties of a small sample of such systems). As previously observed, more than 50% of the intervening systems would require ejection velocities larger than 50,000 km s^{-1}, making an intrinsic origin of these absorbers very unlikely. Recently, Bergeron et al. (2011), based on similar distribution of strong Mg II absorbers along blazars, have suggested a possible theoretical model for producing such high relative velocities.

The red curves represent similar quantities from our Monte Carlo analysis of the QSO sight lines. A K-S test analysis shows for both metrics that the GRB and QSO absorbers are consistent with having been drawn from the same parent population ($P_{KS} = 0.48$ and $P_{KS} = 0.39$, for the W_r and the projected velocity, respectively).

6. DISCUSSION AND CONCLUSION

We have presented the largest compilation to date of GRB spectroscopic data, more than 100 spectra including data from previous published works, proprietary data sets, and publicly

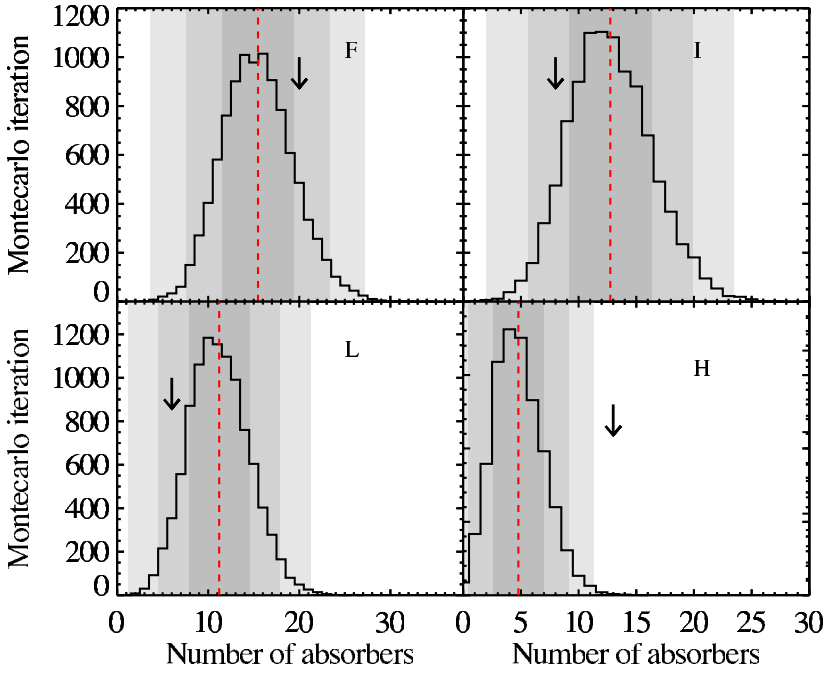

Figure 8. Black curves show the distribution of recovered Mg II absorbers along Monte Carlo realizations of quasar sight lines designed to match the $g(z)$ survey path of the GRB samples (from top left clockwise, Sample F, Sample I, Sample L, and Sample H). The red dashed lines trace the mean number of absorbers for each distribution and the shaded regions represent the 1σ, 2σ, and 3σ confidence interval assuming Poisson statistics. The solid arrow in each panel denotes the number of Mg II absorbers detected for each subsample of GRBs. Only the high-resolution Sample H exhibits a statistically significant excess, but we caution that this sample has substantial overlap with the original P06 work.

(A color version of this figure is available in the online journal.)

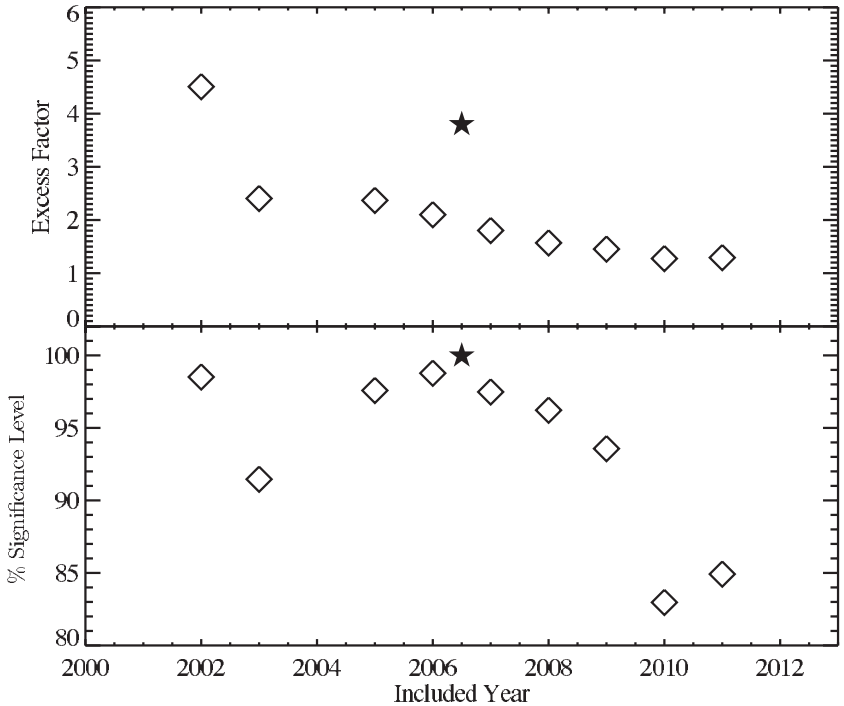

Figure 9. Top: observed excess in the incidence of strong Mg II absorption along GRB sight lines relative to that predicted from observations along quasar sight lines. This is shown as a function of historical time where each bin includes all the GRB lines of sight until December 31 of the specified year, as extracted from Sample F. The filled star marks the results published by PO6. Bottom: confidence level at which the excess factor has been detected based on the Monte Carlo analysis described in Section 5.2.

available data sets not yet published. We have leveraged this data set to investigate the puzzling excess of strong Mg II absorbers along GRB sight lines as first noted by Prochter et al. (2006b). Most importantly, we have performed such analysis on a fully independent data set to the original P06 study in order to test their findings.

This independent sample, our Sample I, comprises 83 GRB lines of sight, yielding a redshift path length $\Delta z = 44.9$ over the interval $z = 0.36$–2.2. Along these spectra, we detect only eight absorbers, for a total incidence of strong Mg II absorbers ($W_r > 1$ Å) of $\ell(z)_{\rm GRB,I} = 0.18$. This incidence lies in good agreement with estimations along QSO

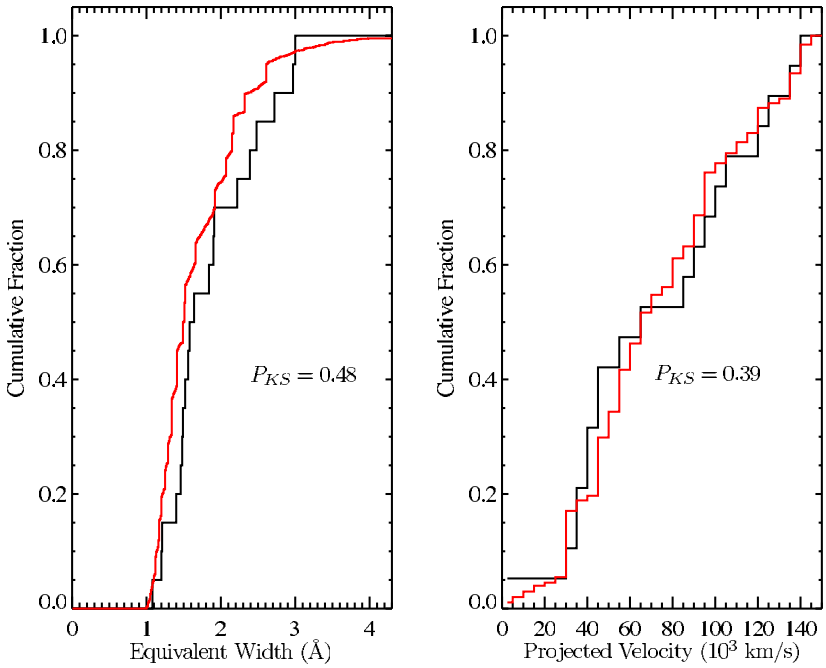

Figure 10. Left: rest-frame cumulative equivalent width distribution of the Mg II absorbers in Sample F (black) and the QSOs absorbers from our Monte Carlo analysis (red). Right: cumulative distribution of the relative velocity (black for the GRB and red for the QSO absorbers), assuming every absorber is local to the QSO or the GRB host galaxy and is moving toward the observer mimicking a foreground intervening system at lower redshift). Kolmogorov–Smirnov tests reveal that the properties of the Mg II absorbers along GRB and QSO sight lines are consistent with having been drawn from the same parent population.

(A color version of this figure is available in the online journal.)

lines of sight taken from the latest work by Zhu & Menard (2012) ($l(z)_{\rm QSO} = 0.26$). No excess has been identified in the independent sample and therefore we do not confirm the original findings of P06 that an excess of Mg II absorbers lie along GRB sight lines.

It is likely that the earlier works on the incidence of Mg II absorption along GRB sight lines were biased by a remarkable, statistical fluke. In particular, the presence of a small set of lines of sight with multiple absorbers appears to have driven the results (as suggested by Kann et al. 2010).

Even including the original P06 data (i.e., our full data set, Sample F), which maximizes the redshift path coverage observed along GRBs sight lines ($\Delta z = 55.5$), we estimate $\ell(z)_{\rm GRB,F} = 0.36 \pm 0.09$, which corresponds to an excess of strong Mg II absorbers by a factor $\sim$1.5 over QSO sight lines (at 90% c.l. for Poisson distribution). We tested the significance of this excess using a Monte Carlo analysis and find that 6% of random QSO samples exhibit as many absorbers as the GRB survey. This suggests the null hypothesis is ruled out at $\lesssim 2\sigma$ confidence level. In conclusion, the data no longer demand a different incidence of strong Mg II absorption along GRB and QSO sight lines.

We emphasize that the P06 analysis was not inherently flawed. Indeed, if we restrict our analysis to the set of high-resolution data, which has large overlap with the P06 sample, we find a significant excess ($\approx$3 times) at a high statistical significance ($\approx 4\sigma$). At face value, this could suggest that we have underestimated $\ell(z)$ for the low-resolution sample, e.g., because we misestimated our sensitivity to 1 Å absorbers. Our sample of low-resolution data, however, includes a large diversity of S/N. In order to investigate the effect of these diversity on our detection rate, we degraded the spectra in Sample H to the lowest S/N and resolution for which we are able to estimate the redshift path length (e.g., the ALFOSC spectrum of GRB 050802, which has S/N = 7 and $R \approx 440$): all the strong Mg II doublets could still be detected at 5σ level. Furthermore, we have identified many additional Mg II absorbers in these spectra (Table 5) where the selection criteria are not fully satisfied. We also established our completeness level and the reliability of our automatic searching algorithm creating a larger ($\sim$5000) set of spectra, derived by the original full sample, where we randomly injected mocked doublet profiles with different equivalent widths. Figure 5 shows that there is no difference in the injected and recovered equivalent width distributions when considered low-resolution and high-resolution subsamples of the mock spectra. Overall, the automatic identification process recovered $\sim$98% of the mocked features. At this stage, we suspect that the few lines of sight observed with high-resolution spectrographs were simply "peculiar" with respect the presence of strong Mg II doublets. Surely a larger collection of such data (e.g., the sample building with X-Shooter) will allow for an independent test of the high-resolution results.

It is also worth noting, in this context, that other authors have explored whether the brightness of the GRB afterglow correlates with the presence of intervening Mg II absorption, i.e., to bias the observations toward such sight lines. Kann et al. (2010) have investigated the optical properties of these GRBs in relation to the presence/absence of Mg II absorbers and the possibility that GRB optical afterglows brightness may be boosted due to gravitational lensing (see Porciani et al. 2007b; Ménard et al. 2008). In particular, they compared the absolute mean B-band magnitude (estimated at one day post-burst and normalized at $z = 1$) of GRB with strong absorbers and without (which usually present weak absorbers). For this purpose, they used afterglow spectra obtained with echelle spectrographs which provide high S/N. No appreciable difference was noticed between the two samples. While we defer the reader to Ménard (2005) for a quantitative estimate of possible gravitational lensing effects, we note that considering only the lines of sight with strong absorbers, our Sample H extends the original work of Kann et al.

(2010) by only one object, leading to inconclusive progress on this aspect due small size samples.

Moreover, we compared the equivalent width distribution of the detected absorbers in our Sample F and our Monte Carlo analysis: a K-S test shows that no significant difference is present between the two samples ($P_{KS} = 0.48$). Similarly, if considering the relative velocity of the two populations of absorbers as they were, instead of intervening, moving at high velocity toward the observer so as to mimic a lower redshift we also do not find any particular difference ($P_{KS} = 0.39$), further disfavoring an intrinsic nature for the absorbers.

Undoubtedly, the most robust results are obtained from high S/N, high-resolution (Echelle or Echellette) data, of which we only have a limited sample for GRB afterglows to date. For this reason, new samples (such as that being gathered by X-shooter) obtained at high resolution will provide an important test of our conclusions.

A.C. thanks the anonymous referee for the valuable comments and suggestions. A.C. also thanks J.X. Prochaska for the fundamental guidances, without which this work could not be possible. A.C. also thanks B. Menard and B. Zhu for the useful comments and to have provided the best to date compilation of high signal-to-noise quasars spectra as well their Mg II search results. Gemini results are based on observations obtained at the Gemini Observatory, which is operated by the Association of Universities for Research in Astronomy, Inc., under a cooperative agreement with the NSF on behalf of the Gemini partnership: the National Science Foundation (United States), the National Research Council (Canada), CONICYT (Chile), the Australian Research Council (Australia), Ministério da Ciência, Tecnologia e Inovação (Brazil), and Ministerio de Ciencia, Tecnología e Innovación Productiva (Argentina). S.L. has been supported by FONDECYT grant number 1100214 and received partial support from the Center of Excellence in Astrophysics and Associated Technologies (PFB 06). J.P.U.F. acknowledges support from the ERC-StG grant EGGS-278202. The Dark Cosmology Centre is funded by the DNRF.

REFERENCES

Barth, A. J., Sari, R., Cohen, M. H., et al. 2003, ApJL, 584, L47
Barthelmy, S. D., Butterworth, P., Cline, T. L., et al. 1995, Ap&SS, 231, 235
Barton, E. J., & Cooke, J. 2009, AJ, 138, 1817
Bergeron, J. 1986, A&A, 155, L8
Bergeron, J., Boissé, P., & Ménard, B. 2011, A&A, 525, A51
Bordoloi, R., Lilly, S. J., Knobel, C., et al. 2011, ApJ, 743, 10
Bowen, D. V., Blades, J. C., & Pettini, M. 1995, ApJ, 448, 634
Bowen, D. V., & Chelouche, D. 2011, ApJ, 727, 47
Budzynski, J. M., & Hewett, P. C. 2011, MNRAS, 416, 1871
Castro, S., Galama, T. J., Harrison, F. A., et al. 2003, ApJ, 586, 128
Cenko, S. B., Fox, D. B., Penprase, B. E., et al. 2008, ApJ, 677, 441
Chen, H.-W. 2012, MNRAS, 419, 3039
Chen, H.-W., Helsby, J. E., Gauthier, J.-R., et al. 2010, ApJ, 714, 1521
Chen, H.-W., Perley, D. A., Pollack, L. K., et al. 2009, ApJ, 691, 152
Chen, H.-W., & Tinker, J. L. 2008, ApJ, 687, 745
Christensen, L., Fynbo, J. P. U., Prochaska, J. X., et al. 2011, ApJ, 727, 73
Churchill, C. W., Rigby, J. R., Charlton, J. C., & Vogt, S. S. 1999, ApJS, 120, 51
Cooksey, K. L., Thom, C., Prochaska, J. X., & Chen, H.-W. 2010, ApJ, 708, 868
Cucchiara, A. 2010, PhD thesis, The Pennsylvania State University
Cucchiara, A., Cenko, S. B., Bloom, J. S., et al. 2011a, ApJ, 743, 154
Cucchiara, A., Jones, T., Charlton, J. C., et al. 2009, ApJ, 697, 345
Cucchiara, A., Levan, A. J., Fox, D. B., et al. 2011b, ApJ, 736, 7
de Ugarte Postigo, A., Fynbo, J. P. U., Thöne, C. C., et al. 2012, A&A, 548, A11
de Ugarte Postigo, A., Thöne, C. C., Goldoni, P., & Fynbo, J. P. U. X-shooter GRB Collaboration 2011, AN, 332, 297
D'Elia, V., Campana, S., Covino, S., et al. 2011, MNRAS, 418, 680
D'Elia, V., Fynbo, J. P. U., Covino, S., et al. 2010, A&A, 523, A36
Frank, S., Bentz, M. C., Stanek, K. Z., et al. 2007, Ap&SS, 312, 325
Fynbo, J. P. U., Jakobsson, P., Prochaska, J. X., et al. 2009, ApJS, 185, 526
Gehrels, N., Chincarini, G., Giommi, P., et al. 2004, ApJ, 611, 1005
Gehrels, N., Ramirez-Ruiz, E., & Fox, D. B. 2009, ARA&A, 47, 567
Goldoni, P., Royer, F., François, P., et al. 2006, Proc. SPIE, 6269, 80
Greiner, J., Bornemann, W., Clemens, C., et al. 2008, PASP, 120, 405
Hook, I. M., Jørgensen, I., Allington-Smith, J. R., et al. 2004, PASP, 116, 425
Horne, K. 1986, PASP, 98, 609
Jakobsson, P., Fynbo, J. P. U., Ledoux, C., et al. 2006, A&A, 460, L13
Jakobsson, P., Hjorth, J., Fynbo, J. P. U., et al. 2004, A&A, 427, 785
Kacprzak, G. G., Churchill, C. W., & Nielsen, N. M. 2012, ApJL, 760, L7
Kacprzak, G. G., Churchill, C. W., Steidel, C. C., & Murphy, M. T. 2008, AJ, 135, 922
Kann, D. A., Klose, S., Zhang, B., et al. 2010, ApJ, 720, 1513
Kawai, N., Kosugi, G., Aoki, K., et al. 2006, Natur, 440, 184
Klose, S., Greiner, J., Rau, A., et al. 2004a, AJ, 128, 1942
Klose, S., Greiner, J., Rau, A., et al. 2004b, AJ, 128, 1942
Lanzetta, K. M., Turnshek, D. A., & Wolfe, A. M. 1987, ApJ, 322, 739
Lawther, D., Paarup, T., Schmidt, M., et al. 2012, A&A, 546, A67
López, G., & Chen, H.-W. 2012, MNRAS, 419, 3553
Matejek, M. S., & Simcoe, R. A. 2012, ApJ, 761, 112
Ménard, B. 2005, ApJ, 630, 28
Ménard, B., Nestor, D., Turnshek, D., et al. 2008, MNRAS, 385, 1053
Ménard, B., Wild, V., Nestor, D., et al. 2011, MNRAS, 417, 801
Metzger, M. R., Djorgovski, S. G., Kulkarni, S. R., et al. 1997, Natur, 387, 878
Milvang-Jensen, B., Fynbo, J. P. U., Malesani, D., et al. 2012, ApJ, 756, 25
Mirabal, N., Halpern, J. P., Kulkarni, S. R., et al. 2002, ApJ, 578, 818
Nestor, D. B., Johnson, B. D., Wild, V., et al. 2011, MNRAS, 412, 1559
Nestor, D. B., Turnshek, D. A., & Rao, S. M. 2005, ApJ, 628, 637
Perley, D. A., Li, W., Chornock, R., et al. 2008, ApJ, 688, 470
Pollack, L. K., Chen, H.-W., Prochaska, J. X., & Bloom, J. S. 2009, ApJ, 701, 1605
Porciani, C., & Madau, P. 2001, ApJ, 548, 522
Porciani, C., Viel, M., & Lilly, S. J. 2007a, ApJ, 659, 218
Porciani, C., Viel, M., & Lilly, S. J. 2007b, ApJ, 659, 218
Prochaska, J. X., Chen, H.-W., & Bloom, J. S. 2006, ApJ, 648, 95
Prochaska, J. X., Chen, H.-W., Bloom, J. S., et al. 2007, ApJS, 168, 231
Prochter, G. E., Prochaska, J. X., & Burles, S. M. 2006a, ApJ, 639, 766
Prochter, G. E., Prochaska, J. X., Chen, H.-W., et al. 2006b, ApJL, 648, L93
Quider, A. M., Nestor, D. B., Turnshek, D. A., et al. 2011, AJ, 141, 137
Rapoport, S., Onken, C. A., Schmidt, B. P., et al. 2012, ApJ, 754, 139
Rapoport, S., Onken, C. A., Wyithe, J. S. B., Schmidt, B. P., & Thygesen, A. O. 2013, ApJ, 766, 23
Rodríguez Hidalgo, P., Wessels, K., Charlton, J., et al. 2012, MNRAS, 427, 1801
Rubin, K. H. R., Prochaska, J. X., Ménard, B., et al. 2011, ApJ, 728, 55
Salvaterra, R., Della Valle, M., Campana, S., et al. 2009, Natur, 461, 1258
Schneider, D. P., Hartig, G. F., Jannuzi, B. T., et al. 1993, ApJS, 87, 45
Schulze, S., Fynbo, J. P. U., Milvang-Jensen, B., et al. 2012, A&A, 546, 20
Simcoe, R. A., Cooksey, K. L., Matejek, M., et al. 2011, ApJ, 743, 21
Steidel, C. C. 1993, in ASP Conf. Ser. 49, Galaxy Evolution. The Milky Way Perspective, ed. S. R. Majewski (San Francisco, CA: ASP), 227
Steidel, C. C., & Sargent, W. L. W. 1992, ApJS, 80, 1
Stocke, J. T., & Rector, T. A. 1997, ApJL, 489, L17
Tanvir, N. R., Fox, D. B., Levan, A. J., et al. 2009, Natur, 461, 1254
Tejos, N., Lopez, S., Prochaska, J. X., Chen, H.-W., & Dessauges-Zavadsky, M. 2007, ApJ, 671, 622
Tejos, N., Lopez, S., Prochaska, J. X., et al. 2009, ApJ, 706, 1309
Thoene, C. C., de Ugarte Postigo, A., Vreeswijk, P. M., Malesani, D., & Jakobsson, P. 2008, GCN, 8058, 1
van Dokkum, P. G. 2001, PASP, 113, 1420
Vergani, S. D., Petitjean, P., Ledoux, C., et al. 2009, A&A, 503, 771
Vestrand, W. T., Borozdin, K. N., Brumby, S. P., et al. 2002, Proc. SPIE, 4845, 126
Vreeswijk, P. M., Ellison, S. L., Ledoux, C., et al. 2004, A&A, 419, 927
Vreeswijk, P. M., Ledoux, C., Smette, A., et al. 2007, A&A, 468, 83
Vreeswijk, P. M., Møller, P., & Fynbo, J. P. U. 2003, A&A, 409, L5
Werk, J. K., Prochaska, J. X., Thom, C., et al. 2012, ApJS, 198, 3
York, D. G., Adelman, J., Anderson, J. E., Jr., et al. 2000, AJ, 120, 1579
Zhu, G. B., & Menard, B. 2012, ApJ, 770, 130
Zibetti, S., Ménard, B., Nestor, D. B., et al. 2007, ApJ, 658, 161